Ligand-Coupled Conformational Changes in a Cyclic Nucleotide-Gated Ion Channel Revealed by Time-Resolved Transition Metal Ion FRET

Pierce Eggan[a], Sharona E. Gordon[a],*, William N. Zagotta[a],*

Author affiliations

[a]Department of Physiology and Biophysics, University of Washington, Seattle, WA 98195

Corresponding authors

*Sharona E. Gordon, Ph.D., Department of Physiology and Biophysics, University of Washington, Seattle, WA 98195-7290, Phone: (206) 616-4861 Email: seg@uw.edu

*William N. Zagotta, Ph.D., Department of Physiology and Biophysics, University of Washington, Seattle, WA 98195-7290, Phone: (206) 685-3878 Email: zagotta@uw.edu

Author contributions

PE, SEG, WNZ designed experiments, performed research, analyzed data, and wrote the paper.

Competing interests

The authors declare no competing interest.

Keywords

CNG channel, allostery, conformational dynamics

Abstract

Cyclic nucleotide-binding domain (CNBD) ion channels play crucial roles in cellular-signaling and excitability and are regulated by the direct binding of cyclic adenosine- or guanosine-monophosphate (cAMP, cGMP). However, the precise allosteric mechanism governing channel activation upon ligand binding, particularly the energetic changes within domains, remains poorly understood. The prokaryotic CNBD channel SthK offers a valuable model for investigating this allosteric mechanism. In this study, we investigated the conformational dynamics and energetics of the SthK C-terminal region using a combination of steady-state and time-resolved transition metal ion Förster resonance energy transfer (tmFRET) experiments. We engineered donor-acceptor pairs at specific sites within a SthK C-terminal fragment by incorporating a fluorescent noncanonical amino acid donor and metal ion acceptors. Measuring tmFRET with fluorescence lifetimes, we determined intramolecular distance distributions in the absence and presence of cAMP or cGMP. The probability distributions between conformational states without and with ligand were used to calculate the changes in free energy (ΔG) and differences in free energy change ($\Delta\Delta G$) in the context of a simple four-state model. Our findings reveal that cAMP binding produces large structural changes, with a very favorable $\Delta\Delta G$. In contrast to cAMP, cGMP behaved as a partial agonist and only weakly promoted the active state. Furthermore, we assessed the impact of protein oligomerization and ionic strength on the structure and energetics of the conformational states. This study demonstrates the effectiveness of time-resolved tmFRET in determining the conformational states and the ligand-dependent energetics of the SthK C-terminal region.

Significance Statement

Allosteric regulation is pivotal for the function of most proteins, especially ion channels like the cyclic nucleotide-binding domain (CNBD) channels. This study examines the allosteric mechanism of ligand binding in the C-terminal region of the prokaryotic CNBD ion channel SthK using steady-state and time-resolved tmFRET. We uncovered significant structural and energetic changes induced by ligand binding with the full-agonist cAMP and the weak partial agonist cGMP. Our approach also highlights the effectiveness of using fluorescence lifetimes to reveal conformational heterogeneity and free energy changes in proteins. These findings deepen our understanding of CNBD channel activation overall and lay the groundwork for a more comprehensive characterization of the effects of mutations and pharmacological agents in these channels.

Introduction

CNBD channels, part of the voltage-gated ion channel superfamily, play pivotal roles in sensory perception, signal transduction and cellular excitability (1). The CNBD family includes cyclic nucleotide-gated (CNG) channels, which are responsible for visual and olfactory signal transduction, and hyperpolarization-activated cyclic nucleotide-gated (HCN) channels, which regulate the pacemaker activity of the heart (2–4). Despite their diverse physiological roles, CNBD channels all possess a shared tetrameric structure with four identical or similar subunits surrounding a central ion-conducting pore. Each subunit contains three regions: an N-terminal region, a transmembrane region with a voltage-sensor and pore domain, and a cytosolic C-terminal region that consist of a CNBD plus a C-linker connecting the CNBD to the pore (5). These channels are activated by the binding of cyclic nucleotides (such as cAMP or cGMP) to the CNBD, which induces conformational changes throughout the protein structure to ultimately open the pore. This ligand-induced allosteric opening is still poorly understood, and questions remain about the structural and energetic changes that occur during this allosteric regulation. In particular, what are the energetics of the conformational changes in individual domains, how are these conformational changes coupled within and between subunits, and how do these processes differ for full and partial agonists?

SthK is a prokaryotic member of the CNBD family from *Spirochaeta thermophila,* which has considerable sequence and structural similarity to eukaryotic CNBD channels and offers a powerful model for better understanding the allosteric regulation in these channels (6). It is easily expressed in *E.coli*, has established biochemical purification methods, and its physiological properties have been studied with ion flux assays and patch-clamp electrophysiology (7, 8). We have also characterized a cysteine-free version of the protein (cfSthK) and found it to behave nearly identically to wild-type channels, making it amenable to thiol-based site-specific labeling (7). As previously shown, binding of cAMP to SthK causes robust channel currents in *E.coli* spheroplasts (Fig. 1A) with a high degree of cooperativity (Fig. 1B; Hill slope, h: 2.9 ± 0.2) (7). In contrast, cGMP appears to be a poor partial agonist for SthK, and its binding to the same structural pocket is only weakly coupled to conformational changes that increase channel open probability (Fig. 1B).

X-ray crystallography and cryo-EM structures of SthK reveal notable ligand-induced structural changes throughout the protein, particularly in the CNBD (9–11). These differences include a rotation of the CNBD C-helix towards the β-roll upon binding of cyclic nucleotide. This important conformational change is thought to be coupled to a rearrangement of the C-linker, and ultimately to the opening of the pore. However, structures alone have not been able to fully characterize the energetic landscape of the allosteric regulation, especially in determining the structural heterogeneity within conformational states and the energetics between states.

To link structural information to the mechanism of allostery, we used a simple four-state model to describe the conformational states and energetics in the C-terminal of SthK (Fig. 1C). This framework has been used previously to describe allosteric proteins generally and the ligand-binding domains of CNBD channels in particular (12–17). In this model, the CNBD can exist in either resting or active conformational states, both of which can be ligand free (apo) or ligand bound (holo). Whereas in the absence of ligand the transition from resting to active is unfavorable, the presence of agonist (either full or partial) makes the active state more favorable. The equilibrium constants, and therefore energetics, that describe the transitions between states determine the steady-state fraction of molecules in each given state. Using the four-state

energetic model as a framework and an experimental method for determining the fraction of molecules in each state, we can calculate the changes in free energy (ΔG) and differences in energy change (ΔΔG) between the conformational states of the CNBD upon binding of ligands like cAMP and cGMP.

A complex protein, such as an ion channel, consists of multiple domains, each of which can undergo conformational changes that are coupled to ligand binding, transmembrane voltage, or the state of a neighboring domain (18, 19). For example, allostery in CNBD channels can be modeled as a cyclic nucleotide-dependent conformational change in each subunit CNBD that is coupled to a concerted conformational change in the C-linker, which in turn is coupled to a opening conformational change in the pore (1, 12). In this context, to truly understand the allosteric mechanism in CNBD channels, we would need to know ΔG and ΔΔG for each of these domains. Therefore, we need a method that can measure the conformational energetics in each protein domain.

In this study, we utilized our recently described steady-state and time-resolved tmFRET methods to measure the energetics in an isolated C-terminal fragment of SthK (20–22). In tmFRET, a donor fluorophore is paired with a transition metal ion, such as Cu^{2+}, Fe^{2+}, or Ru^{2+}, as an acceptor. Donor-acceptor pairs can then be incorporated in a protein at different residue positions. As in classical FRET with two fluorophores, the efficiency of energy transferred between the donor fluorophore and acceptor metal ion is steeply distance dependent and can be used as a molecular ruler to measure distances between sites on a protein, and therefore conformational changes (23).

In time-resolved tmFRET, changes in fluorescence lifetimes of the donor fluorophore are quantified to report FRET efficiencies, and therefore molecular distances between the donor and acceptor. The fluorescence lifetime is the time, in nanoseconds, between excitation of the donor fluorophore and emission of a photon (23). Unlike steady-state FRET, time-resolved FRET can provide nanosecond snapshots of the distribution of FRET efficiencies in a sample (20, 22). In the time-domain, a histogram of photon latencies for the simplest lifetimes appears as a single exponential decay (Fig. 1D, black line). FRET resulting from a single donor-acceptor distance also produces lifetimes described by a single exponential decay, but with a time constant that decreases in proportion to the FRET efficiency (Fig. 1D, solid green and red lines). However, in the case of two donor-acceptor distances, such as from two protein conformations, the intensity decay will be double exponential, with contributions from both donor-acceptor distances. The average distance of each component and the fraction among components can be determined by fitting the decay with a double-exponential decay model. The fractional contribution of each lifetime represents the prevalence of each distance, and thus conformational state, in the sample population (Fig. 1D, green-red dashed lifetime is a mix of 20% solid green and 80% solid red lifetimes) (23). Time-resolved tmFRET, therefore, resolves the structural distances and relative abundance of multiple conformational states in a protein sample.

Under physiological conditions, donor-acceptor distances in proteins will typically be heterogeneous and fluorescence lifetime data will reflect this heterogeneity. Thus, we have fit lifetime data with a FRET model that assumes Gaussian distributions of donor-acceptor distances within each state. This heterogeneity can arise from both: 1) backbone and rotameric variations within a given state (the width of each peak, Fig. 1E) and 2) differences between conformational states (relative fraction of the resting, black, and active, red, peaks, Fig. 1E). Heterogeneity between conformational states reflects the proportion of molecules in the resting and active states of the protein, which can then be used to calculate the free energy difference between the states

(ΔG). In this study, we used various donor-acceptor pairs in the CNBD of SthK to measure distance distributions of the C-helix relative to the β-roll in the absence and presence of ligand. Distance distributions were used to determine the energetics for the transitions between conformational states of the four-state model described above. These results provide a more complete understanding of the structural and energetic changes in the CNBD with ligand binding.

Results

We engineered three donor sites for tmFRET experiments into a C-terminal fragment of SthK (SthK$_{C-term}$), comprised of the C-linker and CNBD domains (9). At these sites (359, 361 and 364), we introduced the unnatural amino acid acridon-2-ylalanine (Acd) as a donor fluorophore using amber codon suppression with a previously described tyrosyl tRNA synthetase (22, 24). Incorporation of Acd into stop-codon containing SthK$_{C-term}$ constructs occurred only in the presence of both the amino-acyl tRNA synthetase/tRNA plasmid (RS/tRNA) and the Acd amino acid. SDS-PAGE followed by in-gel fluorescence imaging (SthK$_{C-term}$-S361-TAG) indicated that Acd was site-specifically incorporated into our SthK$_{C-term}$ constructs and the incorporated product was readily purified for use in tmFRET experiments (Fig. 2A).

We introduced metal ion acceptor binding sites for tmFRET using cysteine mutations in SthK$_{C-term}$ for modification with cysteine-reactive metal chelators (TETAC and phenanthroline maleimide (phenM)) bound to different transition metals (Cu^{2+}, Fe^{2+}, and Ru^{2+}). The three different metal ion-acceptor complexes used in this study, [Cu(TETAC)]$^{2+}$, [Fe(phenM)$_3$]$^{2+}$, and [Ru(bpy)$_2$phenM]$^{2+}$, are shown in Figure 2B. The distance dependence of energy transfer between donor and acceptor is described by the Förster equation and is dependent on the overlap between the absorbance spectrum of the acceptor and the emission spectrum of the donor, among other factors (23, 25). Paired with Acd, these transition metal acceptor complexes resulted in distances with 50% energy transfer (R$_0$) at 15.6 Å, 41.8 Å, 43.5 Å for [Cu(TETAC)]$^{2+}$, [Fe(phenM)$_3$]$^{2+}$, and [Ru(bpy)$_2$phenM]$^{2+}$, respectively. Thus, with Acd as a donor, these acceptors allowed us to measure both short (10-20 Å) and long distances (25-50 Å) across SthK$_{C-term}$ (Fig. 2B) (21).

The SthK$_{C-term}$ fragment tetramerizes in solution at higher protein concentrations, even though the transmembrane domains are absent. Although the tetrameric structure is the physiologically relevant state for the channel, tetramerization introduces challenges in minimizing the contribution of inter-subunit FRET measurements where only intra-subunit donor-acceptor pairs are desired. Using tmFRET, which is sensitive to relatively short distances, mitigates but does not eliminate this concern. To avoid potential contributions from inter-subunit FRET, Acd-labeled protein was tetramerized with an excess (at least a 3:1 molar ratio) of wild-type SthK$_{C-term}$ protein (WT; Fig. 2C). WT protein had neither Acd incorporation nor cysteine mutations. This approach ensured that, on average, only one (or fewer) Acd-cysteine-containing subunit was present in each tetramer, and our FRET efficiency measurements would be almost exclusively from donor-acceptor pairs within the same subunit.

Tetrameric SthK$_{C-term}$ was efficiently separated from monomeric protein using size exclusion chromatography (SEC), where tetrameric protein eluted primarily as a single monodispersed peak at 14 mL, as observed by both absorbance at 280 nm and Acd fluorescence (Fig. 2D, closed triangle). We confirmed this large SEC peak corresponded to tetramers of SthK$_{C-term}$ using mass photometry, which reported a mass of ~105 kDa, compared to a predicted

5

mass of 101 kDa (Fig. 2E). At the low concentrations (~10nM) used for mass photometry, a second small peak was observed of ~30kDa, which is below the analytical range for this method. All tmFRET experiments used higher protein concentrations to ensure tetramerization.

Steady-State tmFRET for Determining Weighted-Average Distance Changes

      To resolve the structural changes in tetrameric SthK$_{C-term}$, we characterized steady-state tmFRET using SthK$_{C-term}$-S361Acd-V416C, with a long-distance donor-acceptor pair (Fig. 3A), and SthK$_{C-term}$-Q364Acd-R417C, with a shorter distance pair (Fig. 3C). We used the metal ion acceptors $[Fe(phenM)_3]^{2+}$ and $[Ru(bpy)_2phenM]^{2+}$ for the long-distance pair and $[Cu(TETAC)]^{2+}$ for the short-distance pair. We measured time courses of Acd fluorescence intensity of the cysteine-containing construct, upon addition of the acceptor, relative to protein without the cysteine mutation, measured separately as a negative control. We plotted the ratio of the normalized fluorescence intensity for the two protein samples as $F_{Cys}/F_{No\ Cys}$. The addition of metal acceptor produced pronounced quenching specifically in the cysteine-containing constructs (Fig. 3A,B,C). This fluorescence decrease is indicative of FRET-based quenching of the donor by the metal acceptor, with the FRET efficiency given by $E = 1 - F_{Cys}/F_{No\ Cys}$. The addition of a saturating concentration of cAMP (160 µM) further increased quenching, indicating a greater FRET efficiency in the presence of agonist compared to the apo state. The increased FRET is consistent with a cAMP-induced decrease in donor-acceptor distance as the C-helix moves towards the β-roll. The dependence of the apparent FRET efficiency change on the cAMP concentration was measured for each donor-acceptor pair, then normalized for comparison and fit with the Hill equation (Fig. 3D). The Hill fits obtained from different sites and acceptor metals are in close agreement with one another, suggesting similar binding affinities and that our previous measurements were obtained at saturating concentrations. Additionally, the three Hill fits with slopes, h, ~1 suggest that the cooperativity observed in full-length channel electrophysiology is not observed in the isolated C-terminal fragment. These steady-state tmFRET results across different donor-acceptor sites and acceptor complexes underscore the large conformational change of the C-helix induced by cAMP.

      In addition to measuring the conformational rearrangement with the full agonist cAMP, we also used the partial agonist cGMP. Like cAMP, cGMP increased quenching by our transition metal labels (i.e., increased FRET); however, the increase was much smaller than that produced by cAMP. As discussed above, cGMP is a poor partial agonist of SthK which elicits only a small fraction of the channel current elicited by cAMP (Fig. 1A). The cGMP-induced increase in FRET we observed provides further evidence that cGMP indeed binds to SthK and that cGMP binding causes a conformational change that moves the C-helix closer to the β-roll. These data do not, however, distinguish between 1) cGMP producing a smaller movement relative to cAMP (a distinct state), and 2) cGMP producing the same size movement but with a lower fraction in the active state (different energetics).

      At lower protein concentrations, monomeric SthK$_{C-term}$ protein can be separated from tetrameric protein on SEC. Interestingly, for multiple donor-acceptor sites, steady-state tmFRET measurements consistently revealed higher FRET efficiencies (shorter distances) for monomers than for tetramers, particularly in the apo state (*SI Appendix*, Fig. S1). These experiments suggest that tetramerization destabilizes the resting-to-active transition of the SthK$_{C-term}$ protein. For our remaining experiments, we focused on the conformational changes in the tetrameric state of the protein, which is more physiologically relevant.

Predicted *In-Silico* Distance Distributions

To validate the accuracy of tmFRET in determining donor-acceptor distances and ligand-dependent changes in distances, we compared our data to predictions based on structural models. For each donor-acceptor pair, we modelled the donor and acceptor labels on the resting and active static structures of SthK$_{C-term}$ (PDB: 7RSH and 4D7T, respectively) to obtain *in-silico* weighted rotameric ensembles utilizing a previously described python package, chiLife (Fig. 4A) (9, 11, 26). We then calculated the distance distributions between every Acd rotamer and every acceptor rotamer for both the resting and the active structures within subunits (intra-subunit) and between all other subunits (inter-subunit) (Fig. 4B). The inter-subunit distances predicted by chiLife for these sites were longer than 50 Å, contributing less than 15% FRET efficiency to the intra-subunit FRET in either the resting or active states. This inter-subunit FRET is predicted to be negligible in our experiments with added WT SthK$_{C-term}$.

We compared the intra-subunit chiLife distributions with our measured weighted-average distances predicted from steady-state tmFRET experiments. We calculated the distances from our steady-state FRET experiments using the Förster equation (25) and superimposed them on the distributions from chiLife (Fig. 4B, vertical solid black and red lines). Whereas the distance changes based on our tmFRET measurements were generally similar to the structural predictions, the absolute distances differed by as much as 5 Å. Steady-state tmFRET measurements combine several sources of heterogeneity from the protein into a single weighted average, including the presence of mixed populations of resting and active states. An additional source of uncertainty is the labeling efficiency. If, for example, we assume that 10% of the protein sample in steady-state experiments was not labeled with acceptor (e.g., due to cysteine oxidation), the adjusted weighted-average distances from our experimental data become more similar to predicted peak values (vertical dashed black and red lines). Although overall these average distances are close to the expected distances predicted by the structures, a method for measuring the distance distributions would be desirable.

Time-Resolved tmFRET for Determining Distance Distributions

While steady-state tmFRET shows an *average* FRET efficiency (and weighted-average distance) for all the molecules in the sample, time-resolved measurements of fluorescence lifetimes can be used to measure distance *distributions* in the sample. This approach can account for the two forms of heterogeneity in the protein mentioned earlier (within state and between state heterogeneity), as well as protein not labeled with acceptor. Here, we measured fluorescence lifetimes in the frequency-domain, which can obtain distance distributions utilizing the same principles discussed above for time-domain lifetime measurements (Fig. 1D). Instead of measuring donor emission photons in response to an impulse of excitation light, lifetimes in the frequency-domain quantify the phase shift (phase delay) and decrease in amplitude of response (modulation ratio) of the donor emission as functions of the modulation frequency of a sinusoidally-varying excitation light (22).

We first measured the fluorescence lifetime of SthK$_{C-term}$-S361Acd-V416C in the absence of acceptor. The phase delay and modulation ratio as a function of the modulation frequency of the excitation light are shown as gray symbols in the Weber plot of Figure 5A. We fit these data with a model for a single exponential lifetime with a time constant of 17.2 ± 0.01 ns (n=8, Fig. 5A, grey curves), comparable but a little longer than values seen previously for Acd (~16 ns) (22, 27). When [Fe(phenM)$_3$]$^{2+}$ was added to the protein sample, the average fluorescence lifetime decreased, illustrated by a shift in the phase delay and modulation ratios to higher frequencies in

7

the Weber plot (Fig. 5A, black circles). Adding a saturating concentration of cAMP (1.23 mM), further decreased the average lifetime, indicating increased FRET (Fig. 5A, red circles). This change in lifetime is consistent with steady-state measurements and reflects a decreased distance between the C-helix and the β-roll. In contrast, adding a saturating concentration of cGMP (1.23 mM) instead of cAMP only moderately decreased the fluorescence lifetime, with phase delay and modulation ratio curves falling closer to the apo conditions (Fig. 5A, green circles).

To further validate our lifetime measurements using a different acceptor with a different R_0, we repeated these experiments using $[Ru(bpy)_2phenM]^{2+}$ as the acceptor instead of $[Fe(phenM)_3]^{2+}$. $[Ru(bpy)_2phenM]^{2+}$ also decreased the average fluorescence lifetime in all three conditions (apo, cAMP and cGMP) relative to the donor-only lifetime (Fig. 5B). As expected from the longer R_0 value for Acd-$[Ru(bpy)_2phenM]^{2+}$ compared to Acd-$[Fe(phenM)_3]^{2+}$, $[Ru(bpy)_2phenM]^{2+}$ produced an even greater shift in phase delay and modulation ratio towards higher frequencies compared to $[Fe(phenM)_3]^{2+}$ (Fig. 5B, 6B). Neither $[Fe(phenM)_3]^{2+}$ nor $[Ru(bpy)_2phenM]^{2+}$ produced a change in lifetime for SthK$_{C-term}$-S361Acd (without the cysteine) used as a negative control (*SI Appendix,* Fig. S2). The decreases in lifetimes of SthK$_{C-term}$-S361Acd-V416C with the metal acceptors and ligands reflect measurable decreases in the donor-acceptor distances (i.e., conformational state) with the addition of cyclic nucleotide, as seen with the steady-state tmFRET measurements.

To obtain distance distributions and average distances that reflect individual conformational states, we fit our lifetime data to a previously described model that assumes each ligand condition (apo, cAMP and cGMP) is described by a single Gaussian distribution of distances (parameters in *SI Appendix,* Fig. S3) (20). The $[Fe(phenM)_3]^{2+}$ and $[Ru(bpy)_2phenM]^{2+}$ time-resolved tmFRET datasets for each ligand condition were individually fit using this lifetime model (solid and dashed curves, Fig. 5A and B) (20, 22). The average distances ($\bar{r}$) and standard deviations (σ) of the Gaussian distance distributions from these fits are shown for $[Fe(phenM)_3]^{2+}$ and for $[Ru(bpy)_2phenM]^{2+}$ as spaghetti plots experiments in Figures 5C, and 5D, respectively. Overlayed on the spaghetti plots are the distance distributions for the resting and active states predicted using chiLife (dashed curves). The $\bar{r}$ and σ of the lifetime model from individual experiments for apo, cAMP and cGMP are summarized in Figure 5E and F. Average Gaussian distances measured from experiments for apo and cAMP using both $[Fe(phenM)_3]^{2+}$ (apo= 39.6 Å, cAMP= 29.4 Å) and $[Ru(bpy)_2phenM]^{2+}$ (apo= 40.1 Å, cAMP= 29.4 Å) agreed remarkably well with the chiLife predictions and with each other despite the difference in R_0 between $[Fe(phenM)_3]^{2+}$ and $[Ru(bpy)_2phenM]^{2+}$. Interestingly, the cGMP data had an $\bar{r}$ distance between the apo and cAMP $\bar{r}$ values and had a much wider σ, spanning a distance range of the apo and cAMP Gaussians combined.

While this lifetime model, with a single average distance for each ligand condition, fits the time-resolved tmFRET data well, it seems likely that there might be more than one conformational state (resting and active) present for each ligand condition (12). As our four-state model suggests, each liganded condition (apo, cAMP and cGMP) should be comprised of a mixture of resting and active conformational states at varying proportions. For example, the wide cGMP Gaussian positioned between those of the apo and cAMP distributions might reflect the sum of two Gaussians, one with a longer average distance (resting conformation) and one with a shorter average distance (active conformation). The larger apo state σ compared to the chiLife prediction could also be due to the presence of a small fraction of the active state, even without ligand. Determining the fractional occupancy among the resting and active states in the apo,

cAMP and cGMP conditions would provide energetic information about the transition between resting and active SthK$_{C-term}$ in the different conditions.

Global Fitting [Fe(PhenM)$_3$]$^{2+}$ and [Ru(Bpy)$_2$PhenM]$^{2+}$ for Energetic Information

Our approach to measuring fluorescence lifetimes also provides a model-independent way to visually estimate the probability distribution among resting and active states using a representation of the data known as a phasor plot. Phasor plots show the in-phase (*D*) and out-of-phase (*N*) components that underlie the phase delays and modulation ratios shown in the Weber plots (28). The location of the data on the phasor plot allows us to view complex lifetimes without assumptions about the shape of the distance distributions.

The phasor plot for SthK$_{C-term}$-S361Acd-V416C modified by [Fe(phenM)$_3$]$^{2+}$ is shown in Figure 6A. Single-exponential fluorescence lifetimes fall on the universal circle in phasor plots, and for donor-only SthK$_{C-term}$-S361Acd-V416C, the lifetime data fell on the universal circle at 17 ns (Fig. 6A, grey marked with arrow). When fluorescence lifetimes are multi-exponential or nonexponential, the decay data fall inside the universal circle. The data from apo, cAMP, and cGMP conditions all reside within the circle reflecting their complex mixtures of distances. A saturating concentration of cGMP (Fig. 6A, green) gives data that lay on a line connecting the apo data (Fig. 6A, black) and the cAMP data (Fig. 6A, red). This is expected if the cGMP data arises from a mixture of the same distributions found in the apo and cAMP conditions. In contrast, if cGMP were to produce a distinct conformational state with its own donor-acceptor distance, the data would be predicted to lie off the line connecting apo and saturating cAMP concentrations. Using subsaturating concentrations of cAMP illustrates this point as these data also lay along the line connecting apo and saturating cAMP (*SI Appendix,* Fig. S4). Based on these results, we conclude that the active state produced by cGMP is structurally similar to that produced by cAMP, which is consistent with the previous X-ray crystal structures of C-terminal SthK with cAMP and cGMP (9). Although the active state is the same, there must be a higher fraction of protein in the resting state in the presence of cGMP compared to cAMP.

To quantify the fraction of resting and active state in apo, cAMP, and cGMP, we next analyzed our lifetime data by globally fitting them to the lifetime model for Gaussian distributions of distances (*SI Appendix,* Fig. S3). The determination of distance distributions from lifetime experiments alone is an ill-posed problem (23). Using global fits of multiple data sets using three different conditions (apo, cAMP, and cGMP) and two different acceptors with different R$_0$s increases our ability to determine the various free parameters. For our global fitting analysis, we assumed that the acceptor complexes [Fe(phenM)$_3$]$^{2+}$ and [Ru(bpy)$_2$phenM]$^{2+}$ would produce the same measured distance distribution (both within states and between states) for the same acceptor site. This is a reasonable assumption given that: 1) the chemical structures of the complexes are very similar (Fig. 2B); 2) chiLife modeling of these two different acceptors produced nearly identical distance distributions (Fig. 4B); and 3) dose-response curves for cAMP measured using steady-state FRET were comparable for [Fe(phenM)$_3$]$^{2+}$- and [Ru(bpy)$_2$phenM]$^{2+}$-modified protein (Fig. 3D). Parameter identifiability for this lifetime model was observed in graphs of χ^2 minimized curves as functions of fixed ranges of each parameter, where minima for each parameter were resolved (*SI Appendix*, Fig. S5). This global fitting allowed us to determine the fraction of resting and active components, and therefore the free energy change, in each condition.

We globally fit six data sets (each set included phase delay and modulation ratio data), representing the conditions of apo, cAMP and cGMP with the two different acceptors

[Fe(phenM)$_3$]$^{2+}$ and [Ru(bpy)$_2$phenM]$^{2+}$. We parameterized the distance distribution as the sum of two Gaussians. Each of the Gaussian parameters $\overline{r_1}$, $\overline{r_2}$, σ_1, and σ_2 were assumed to be the same across all conditions, and the fraction of each Gaussian (set by parameter A_2) was allowed to vary between conditions. Global fitting of the lifetime model provided an excellent fit to all of the data (Fig. 6B) revealing the distance distributions shown in Figure 6C. Similar to the chiLife predictions (Fig. 4) and the single Gaussian fits (Fig. 5), the global fits gave $\overline{r_1}$ and $\overline{r_2}$ values of 40.9 Å and 29.5 Å in the resting and active states, respectively, with σ_1 and σ_2 values of 4.3 Å and 0.84 Å in the resting and active states, respectively (Fig. 6C, D). Surprisingly, our fits indicated that the apo condition is best explained with 12% in the active state ($A_2 = 0.12$) and 88% in the resting state, whereas the saturating cAMP concentration condition was best fit with only the active state ($A_2 = 1$) (Fig. 6E). In contrast, cGMP was fit with an A_2 of 0.34. Given that the qualities of these fits are comparable to the single Gaussian fits (with similar χ^2 values), and fewer parameters were used in the global fits than across the sum of comparable data sets with single Gaussian fits, we find the global fitting approach more parsimonious with the phasor plot data and previous SthK X-ray crystallography data in cGMP (9).

Using the probabilities of resting and active states in each condition and the Gibbs free energy equation, we calculated the ΔG and $\Delta\Delta G$ energetics of the transitions in the four-state diagram (Fig. 1C and Table 1). In the absence of cyclic nucleotide, the lifetime model fit gave an A_2 of 0.12, corresponding to a ΔG_{Apo} of 1.2 kcal/mol. The isolated SthK$_{C-term}$, therefore, exhibits considerable activation even in the apo state. For saturating cAMP, for which the global fit indicated an A_2 of 1, we assumed a maximum contribution of the resting state of 0.01, yielding a ΔG_{cAMP} that is more favorable than -2.7 kcal/mol and a $\Delta\Delta G_{cAMP}$ that is more favorable than -3.9 kcal/mol. With a $\Delta\Delta G_{cGMP}$ of -0.82 kcal/mol, cGMP was found here to be a partial agonist, consistent with electrophysiology and previous experiments (7, 8, 10). Interestingly, our measurements reporting the conformational change in the isolated CNBD show a greater activation for apo, cAMP and cGMP, than electrophysiology experiments on full-length channels. These results demonstrate that time-resolved tmFRET can be utilized to obtain energetic information on the individual domains during the allosteric activation of SthK.

Changes in Energetics with Salt Concentrations

We were surprised by the high probability of being in the active state for cGMP ($A_2 = 0.34$) indicated by the sum of Gaussian fits (Fig. 6E), especially when electrophysiology shows a much lower open probability with cGMP (Fig. 1A). Although this difference might be due to intrinsic energetic differences between our fragment SthK$_{C-term}$ construct and the full-length channel, it could also arise, in part, from the high ionic conditions (500 mM) used in our lifetime experiments compared with physiological ionic concentrations used in electrophysiology experiments. Known inter-subunit C-terminal salt bridge interactions could be destabilized by increased ionic strength and, previously, it was observed that higher ionic strength eliminated tetramerization in HCN1 C-terminal fragments (7, 29, 30). However, we found no difference in elution volume for SEC experiments performed with SthK$_{C-term}$-S361Acd-V416C using 150 mM instead of 500 mM KCl, indicating that the oligomerization state was the same under both experimental conditions (Fig. 7A).

To test whether the high ionic strength of our experiments contributed to the high A_2 for cGMP, we repeated the above lifetime experiments with a more physiological salt concentration (150 mM KCl). We made new time-resolved tmFRET measurements with SthK$_{C-term}$-S361Acd-V416C in lower ionic conditions, for both the [Fe(phenM)$_3$]$^{2+}$ and [Ru(bpy)$_2$phenM]$^{2+}$ acceptors

10

across apo, cAMP and cGMP conditions. Comparison of $[Fe(phenM)_3]^{2+}$ lifetime data in the two different ionic conditions are shown in the representative Weber plot in Figure 7B. While the apo and cAMP data appeared to be equivalent between 150 and 500 mM KCl, the cGMP data were different between the conditions. When an additional 300 mM KCl was added to protein samples in 150 mM KCl after cGMP application, the phase delay and modulation ratio approached the same lifetimes as the 500 mM KCl cGMP condition (Fig. 7B, dark green circle), recapitulating the 500 mM KCl data set. We then globally fit the 150 mM KCl data across $[Fe(phenM)_3]^{2+}$ and $[Ru(bpy)_2phenM]^{2+}$ acceptors for apo, cAMP and cGMP conditions with the sum of two Gaussians (Fig. 7C), and found that the average distances, $\overline{r}$, and standard deviations, σ, were nearly identical to those at 500 mM KCl (Fig. 7D). The A_2 from cGMP fits decreased in 150 mM KCl compared to 500 mM KCl indicating that a decrease in ionic concentration made activation by cGMP less favorable ($\Delta\Delta G_{cGMP}$ = -0.47 kcal/mol, $\Delta\Delta\Delta G_{cGMP\ KCl}$ = 0.35 kcal/mol). In the absence of ligand, A_2 was unchanged between the two ionic concentrations (Fig. 7D), indicating that the increased ionic strength effected only the active conformation in the presence of cGMP. Since activation is already very favorable in the presence of cAMP, we could not determine if ionic strength also effected $\Delta\Delta G_{cAMP}$. These results suggest that ionic strength might specifically affect an electrostatic interaction between CNBD and the cyclic nucleotide during the activation transition.

Discussion

In this study, we measured both steady-state and time-resolved tmFRET for a C-terminal fragment of SthK and interpreted the data using a four-state allosteric model. This approach allowed us to acquire structural information and energetics of the conformational change of the C-helix under different ligand and experimental conditions. Our findings revealed a small presence of the active state in the absence of ligand, while saturating concentrations of cAMP exhibited energetics consistent with that of a full agonist by strongly shifting occupancy into the active state. In contrast, saturating concentrations of cGMP demonstrated characteristics of a partial agonist, eliciting a lower fraction of the same active conformation observed with cAMP. Furthermore, our results demonstrated the impact of both oligomerization and ionic strength on the energetics of the conformational change of isolated SthK_C-term.

Our ability to recover structural information in the form of average distance, $\overline{r}$, and standard deviation of distances, σ, from time-resolved tmFRET indicates that this approach is superior to weighted-average steady-state distance measurements alone. The average distance values obtained from lifetime measurements closely matched the distances predicted by chiLife, indicating that the characterized states likely correspond to the observed resting and active states in existing X-ray and cryo-EM structures (9, 11). Whereas the active state's standard deviation (σ_2) closely aligned and was slightly narrower than the chiLife predictions, the resting state's standard deviation (σ_1) was larger than chiLife predictions, even with the global fitting approach. This indicates a broad structural heterogeneity in the resting state that cannot be explained by the rotamer clouds of the labels alone, such as heterogeneity in the position of the C-helix backbone, which is consistent with several past experimental observations (10, 31, 32). Overall, time-resolved tmFRET reliably provides valuable, although sparse, structural insights, especially in cases of heterogeneity where current structural methods are limited.

In addition to the heterogeneity within a given conformational state, time-resolved tmFRET allowed us to obtain the heterogeneity between conformational states (A_2) and thus

energetics of state transitions in our four-state model. We determined the distribution between these four conformational states by employing a model comprising the sum of two Gaussian distributions, and globally fitting data across distinct acceptors and ligand conditions. This analysis allowed us to quantify the changes in free energy (ΔG) describing our four-state model. Additionally, we were able to calculate the $\Delta\Delta G$ for each ligand, which represents the free energy imparted by the ligand to drive the conformational change of the CNBD. Although we assumed a model with only two stable conformational states, this may not capture all the stable states in the CNBD. Even if the conformational distributions assumed here were oversimplified, our time-resolved tmFRET approach still allowed for a deeper understanding of the allostery in the C-terminal of SthK.

There are some complications with our time-resolved tmFRET approach that should be considered in future applications. 1) Donor and acceptor sites for tmFRET were carefully selected for solvent accessibility, but it is possible that the introduction of Acd and metal acceptor altered the energetics compared to WT SthK$_{C\text{-term}}$. 2) Incomplete labeling in our protein samples introduces a fraction of donor-only molecules, which are not captured in steady-state measurements but are estimated in our lifetime fits. We have previously shown that there is some degree of correlation among parameters in our FRET model, particularly between the fraction of donor-only and the standard deviation of the Gaussians (22). As a result, it is important to ensure a low contribution (<15%) from the donor-only fraction, and this fraction should be validated by independent methods. 3) Although parameters all reliably converged to χ^2 minimized values in our global fits, some parameters were more identifiable than others (*SI Appendix,* Fig. S5). 4) Both the single Gaussian distribution model and the sum of two Gaussian distributions model yielded minimized χ^2s and excellent fits, however, our results do not conclusively favor one lifetime model over the other. Whereas the single Gaussian distribution fits contain fewer assumptions, the sum of two Gaussian global fits contain fewer free parameters across the multiple acceptors and conditions. We believe that the assumptions in the four-state model and sum of two Gaussians fitting are reasonable based on both previous experiments and theoretical considerations (7, 12, 22).

A number of previous studies have measured the energetics of allostery in CNBD channels, however interpreting our results within the context of these previous studies presents challenges. These studies have utilized various different CNBD channels where the energetics, including even the ligand specificity, are very different (7, 12, 13, 30, 33–38). For example, in CNGA1 channels from rod photoreceptors, cGMP is a full agonist, and cAMP is a weak partial agonist, while in SthK the agonist specificity is reversed (6, 7, 39, 40). In addition, most of these previous studies have been limited to electrophysiology, which measures the open probability of the pore. Without additional information, the open probability provides only an indirect measurement of the energetics of other domains like the ligand-binding domain. While double electron-electron resonance spectroscopy (DEER) (12, 13, 33, 34) and single-molecule fluorescence studies (11, 35, 41) offer the potential to measure the energetics of individual domains, these methods have not yet been applied to the SthK CNBD. Interestingly, DEER spectroscopy on the HCN2 CNBD fragment revealed a mixture of resting and active states in cAMP (12), whereas we observed in the SthK CNBD fragment a more favorable transition in cAMP. These differences might be due to either inherent differences in the energetics between the C-terminal domains of SthK and HCN2, or the different experimental conditions used, such as the monomeric protein used in the DEER studies vs the tetrameric C-terminal domain studied here. Although their energetics may differ, all CNBD channels studied to date appear to involve

an allosteric transition of the CNBD where the binding of cyclic nucleotide promotes a movement of the C-helix relative to the β-roll that is coupled indirectly to the opening of the pore.

For simplicity, here we used the C-terminal fragment of SthK instead of the full-length channel. The relationship between the energetics of the C-terminal fragment and the full-length channel is likely complex and requires further study. For example, coupling of the conformational changes in the individual CNBDs to a concerted opening of the pore is expected to alter both the ΔG for the CNBD transition and the cooperativity of the transitions between subunits. This coupling would also make the ΔΔG measured in the pore by electrophysiology smaller than the ΔΔG we measured in the CNBD. If the conformational change in the CNBD is the same in the fragment and full-length channel, as suggested by structural studies (9, 11), we could use our measured ΔΔG from the fragment, together with measurements from the full-length channel, to develop a full allosteric model of the intact channel.

Materials and Methods

Constructs and Mutagenesis. The C-terminal construct of SthK (SthK$_{C-term}$) was created by replacing the first 224 residues of cysteine-free SthK in the pETM11 vector (described previously, Uniprot accession #E0R11) (7), with the sequence for MBP followed by a 14 residue asparagine linker and a TEV protease cleavage site, using restriction digestion and T4 ligation. Following the C-terminal end of truncated SthK sequence (225-430), another TEV cleavage site and a Twin-Strep-tag sequence was incorporated using Gibson cloning. An amber stop codon (TAG) was introduced at positions 359, 361 or 364 of the WT SthK$_{C-term}$ using site directed mutagenesis (42) to create new "donor-only" constructs. To generate constructs with both donor and acceptor sites, a single cysteine mutation was introduced into each donor-only construct at sites 416 or 417, to make the three constructs: SthK$_{C-term}$-I359TAG-V417C, SthK$_{C-term}$-S361TAG-V416C, and SthK$_{C-term}$-Q364TAG-V417C.

Expression and Purification of the C-Terminal SthK fragment. The WT SthK$_{C-term}$, donor-only, and cysteine-containing constructs were each co-transformed with the AcdA9 aminoacyl tRNA synthetase/tRNA-containing plasmid (pDule2) (43) into B-95.ΔA *E. coli* (DE3) cells(44). The transformed *E. coli* cultures were grown in terrific broth medium at 37° C in 50 μg/ml kanamycin and 60 μg/ml spectinomycin to an OD$_{600}$ ~1.0 before adding Acd (for a final concentration of 0.3 mM), and 0.5 mM isopropyl β-D-1-thiogalactopyranoside (IPTG) for protein induction (27, 45). The cultures were transferred to 18°C to grow an additional 17-19 hours, cells were harvested by centrifugation, and cell pellets were resuspended in lysis buffer (150 mM KCl, 50 mM Tris, 2 mM β-mercaptoethanol, and 10% glycerol, pH 7.4 supplemented with complete mini EDTA-free protease inhibitor cocktail (Pierce, ThermoFisher)). Cell suspensions were lysed on an Avestin EmulsiFlex-C3 cell disruptor three times at 15,000- 20,000 psi, then diluted with lysis buffer and cleared by centrifugation at 39,000 x g for 30 minutes. Clarified lysate was loaded onto 0.75 mL of Strep-Tactin Superflow high-capacity beads (iba Biosciences) at 4° C in a disposable column. The resin was washed with 25 column volumes of KBT solution (150 mM KCl, 50 mM Tris, 10% glycerol, pH 7.9) and eluted with 10 mM d-Desthiobiotin (Sigma) in KBT buffer. Eluted protein was treated with 10 mM tris(2-

13

carboxyethyl)phosphine (TCEP) to fully reduce cysteines, flash frozen with liquid nitrogen, and stored at -80° C.

Acd-labeled protein was mixed with WT SthK$_{C-term}$ protein in ratios of >3:1 and were then TEV cleaved with 1:10 vol/vol TEV protease (1.2 mg/ml) for 18 hours at room temperature to cleave the N-terminal MBP and C-terminal Twin-Strep-tag. TEV-cleaved protein was then diluted 1:500 in KBT and then loaded onto a HiTrap Q HP column (GE Healthcare) for ion exchange chromatography (IEC) to remove TEV protease, and cleavage fragments from SthK$_{C-term}$. SthK$_{C-term}$ was eluted with an increasing concentration ramp of KCl (10 mM – 1 M) and fractions were collected, with SthK$_{C-term}$ coming off in a single peak. We used size exclusion chromatography (SEC) on a Superdex 200 10/300 column (GE Healthcare) to evaluate oligomerization state or collect fractions in either KBT or High-KBT (500 mM KCl, 50 mM Tris, 10% Glycerol, pH 7.9).

Mass Photometry. Mass photometry utilizes light scattering to measure the molecular weight of proteins along with their relative abundance in a sample, with an analytical range of 40 kDa - 5 MDa (46, 47). Glass coverslips (24x50 mm) were isopropanol-cleaned and dried with nitrogen gas. We used 10 nM ß-amylase (BAM) to calibrate a TwoMP Mass Photometer instrument (Refeyen Ltd, Oxford, UK). As a background reference, 10 µl of buffer solution (KBT with 150 mM KCl) was first measured in sample gasket wells. Collected SEC SthK$_{C-term}$ fractions were then measured (10 µl added for total of 20 µl, ~50 nM) and mass histograms collected via the DiscoverMP analysis software. The mass histograms were analyzed with single Gaussian fits in IGOR-Pro v.8 (Wavemetrics, Lake Oswego, OR).

Cyclic Nucleotides and Labeling Reagents. Adenosine 3',5'-cyclic monophosphate sodium salt monohydrate (cAMP) and guanosine 3',5'- cyclic monophosphate sodium salt (cGMP) were purchased from Sigma Aldrich and both prepared at 16 mM in 150 mM KCl, 50 mM Tris and 10% glycerol, pH 7.4. Metal acceptor complexes, [Fe(phenM)$_3$]$^{2+}$, [Ru(bpy)$_2$phenM]$^{2+}$, and [Cu(TETAC)]$^{2+}$ for tmFRET were prepared as previously described (21, 22).

SthK$_{C-term}$ Steady-State Fluorescence Measurements. For steady-state tetramer experiments (Fig. 3), fractions from IEC-purified SthK$_{C-term}$ donor-only or SthK$_{C-term}$-Acd-cysteine protein, with excess WT SthK$_{C-term}$, were used at high concentration immediately after elution from the IEC. Protein was confirmed as tetrameric by analytical SEC and diluted 1:2 to 1:5 into KBT into quartz cuvettes. Acd fluorescence intensity was measured at 10 second intervals using Jobin Yvon Horiba FluoroMax-3 spectrofluorometer in anti-photobleaching mode (Edison, NJ) as described previously (20, 21). Acceptor molecules at final concentrations of 6 µM [Fe(phenM)$_3$]$^{2+}$, 20 µM [Ru(bpy)$_2$phenM]$^{2+}$ or 10 µM [Cu(TETAC)]$^{2+}$ were added to the cuvettes followed by 160 µM final concentration of either cAMP or cGMP. For [Cu(TETAC)]$^{2+}$ experiments, 5 mM TCEP was added after cAMP or cGMP to reverse the tmFRET by removing the acceptor. All experiments had a 'no-cysteine' protein control to correct the FRET efficiency for intensity changes without bound acceptor, where FRET efficiency $E = 1 - (F_{Cys}/F_{No\ Cys})$. In different experiments, FRET efficiencies at increasing concentrations of cAMP were normalized to the maximal observed FRET efficiency and experimental averages were fit with the Hill equation. Fit slopes, h, were fixed at 1 for the [Ru(bpy)$_2$phenM]$^{2+}$ and [Cu(TETAC)]$^{2+}$ data but was allowed to vary for the [Fe(phenM)$_3$]$^{2+}$, which did not fit with a slope of 1. For steady-state tmFRET experiments to compare between oligomeric states, monomeric and tetrameric protein

14

were separated and collected by SEC using a Superdex 75 Increase 10/300 GL column (GE Healthcare) and then used directly in fluorescence experiments (*SI Appendix,* Fig. S1).

Measurements of Fluorescence Lifetimes Using FLIM. For lifetime studies, tetrameric SthK$_{\text{C-term}}$-S361Acd-V416C protein, mixed >1:3 with WT SthK$_{\text{C-term}}$, was labeled with either [Fe(phenM)$_3$]$^{2+}$ or [Ru(bpy)$_2$phenM]$^{2+}$. For [Fe(phenM)$_3$]$^{2+}$ experiments, SthK$_{\text{C-term}}$-S361Acd-V416C protein was buffer exchanged using a BioSpin6 Mini column (BioRad) into KBT (150 mM KCl) or High-KBT (500 mM KCl) then labeled immediately prior to lifetime measurements. For [Ru(bpy)$_2$phenM]$^{2+}$ experiments, SthK$_{\text{C-term}}$-S361Acd-V416C protein was incubated with 1 mM [Ru(bpy)$_2$phenM]$^{2+}$ for 30 minutes at room temperature and then buffer exchanged into KBT or High-KBT to remove the unincorporated label.

The theory of time-resolved FRET and the implementation of the lifetime FRET model in the frequency domain have been described previously (23, 48–51). Frequency domain fluorescence lifetime data were obtained using a Q2 laser scanner and A320 FastFLIM system (ISS, Inc., Champaign, IL, USA) attached to a Nikon TE2000U microscope. Acd was excited using a 375 nm pulsed diode laser (ISS, Inc) driven by FastFLIM at 10 MHz, with a long-pass dichroic mirror (387 nM) and a band-pass emission filter (451/106 nm). Collected emission was recorded on a Hamamatsu model H7422P PMT detector. Lifetime measurements were calibrated using Atto 425 in water (with a lifetime of 3.6 ns), using the same optical configuration. Protein samples were used at full strength by pipetting 11 µl onto an ethanol-cleaned #1.5 glass coverslip for recording with a Nikon CFI Super Fluor 10x 0.5NA objective. Confocal images (256 x 256 pixels) were collected with a pinhole of 200 µm and a pixel dwell time of 1 ms. Donor-only lifetimes were obtained from SthK$_{\text{C-term}}$-S361Acd-V416C in KBT and High-KBT solutions prior to the addition of [Fe(phenM)$_3$]$^{2+}$ at a final concentration of 76.8 µM. [Ru(bpy)$_2$phenM]$^{2+}$-labeled protein was measured following buffer exchange. Either 1 µl of 16 mM cAMP or 16 mM cGMP was added to acceptor-labeled protein to a final concentration of 1.23 mM. The phase delays and modulation ratios of the fluorescence signal were obtained using VistaVision software from the sine and cosine Fourier transform of the phase histogram H(p), subject to the instrument response function (20).

Lifetime Distance Distribution Model. The model for obtaining a single Gaussian distribution, or a sum of two Gaussian distributions of distances from lifetimes has been described previously (20, 22). Globally fitting lifetime data across [Fe(phenM)$_3$]$^{2+}$ and [Ru(bpy)$_2$phenM]$^{2+}$ experiments and the conditions of apo, cAMP and cGMP, used the same model as previously described (*SI Appendix*, Fig. S3 for parameters), but parameters were constrained differently. Parameters defining the Gaussian states included: two unconstrained average distances ($\overline{r_1}$ and $\overline{r_2}$), two standard deviations (σ_1 and σ_2) constrained between values of 0.5-10 Å, and one fraction for the proportions between the two Gaussians (A_2) varied independently for each of conditions, apo, cAMP and cGMP, constrained between 0 and 1. Other parameters that were varied independently included: the fraction of donor-only in each respective sample, the fraction of background in each experiment (<5%), and the t$_0$ offset for each experiment. The measured donor-only lifetimes (in KBT and High-KBT) were single exponential, and the time constant was previously measured and held fixed for the global fitting. The acceptor complex R$_0$ values were determined previously (21) and held constant at 41.8 Å and 43.5 Å for [Fe(phenM)$_3$]$^{2+}$ and [Ru(bpy)$_2$phenM]$^{2+}$ respectively[19]. For the single Gaussian lifetime fits, the fraction donor only was held constant within experiments from the same labeled protein samples.

15

Energetic and Hill Equation Calculations. ΔG, $\Delta\Delta G$ and $\Delta\Delta\Delta G$ are calculated as follows:

$$\Delta G = -RT * \ln\left(\frac{P_{active}}{P_{resting}}\right) \tag{1}$$

$$\Delta\Delta G_{cNMP} = \Delta G_{cNMP} - \Delta G_{apo} \tag{2}$$

$$\Delta\Delta\Delta G_{cGMP\ KCl} = \Delta\Delta G_{cGMP\ 150\ mM\ KCl} - \Delta\Delta G_{cGMP\ 500\ mM\ KCl} \tag{3}$$

where R is the molar gas constant, T is the absolute temperature (K), and P_{active} and $P_{resting}$ are the proportion of molecules in the active state and resting respectively, and cNMP is cyclic nucleotide (either cAMP or cGMP).

Hill fits (Fig. 1B and Fig. 3D) were obtained using:

$$Normalized\ Response = 1/\left(1 + (K_{1/2}/[cAMP])^h\right) \tag{4}$$

where $K_{1/2}$ is the concentration of cAMP producing half-maximal FRET change and h is the Hill coefficient.

chiLife Predictions. Computational predictions of the possible rotameric positions for the donor and acceptor labels were made with chiLife using the accessible-volume sampling method as previously described (22, 26). Acd, $[Cu(TETAC)]^{2+}$, $[Fe(phenM)_3]^{2+}$ and $[Ru(bpy)_2phenM]^{2+}$ were added as custom labels in chiLife and modeled onto the cryo-EM structure of the full-length SthK closed state (11) (PDB: 7RSH, residues 225 to 416) and the X-ray crystallography structure of the cAMP bound SthK C-terminal fragment (9) (PDB: 4D7T). For each donor-acceptor pair, labels were superimposed at indicated residue positions and 10,000 possible rotamers were modeled. Rotamers resulting in internal clashes (<2 Å) were removed and external clashes evaluated as previously described (26). Donor-acceptor distance distributions were calculated between the remaining (~500-2000) label rotamers for each donor-acceptor pair. Inter-subunit distances were calculated as distances between one Acd molecule and the modeled acceptor rotamers on each of the other three subunits.

Electrophysiology. The cysteine-free construct of full-length SthK (cfSthK) was cloned into a pcGFP vector (52) (with YFP instead of GFP) and expressed in E.*coli* C43(DE3) bacteria (53). A valine to alanine mutation at position 208 was added for increased open channel probability (A208V-cfSthK-YFP) (7). Spheroplasts were formed from the C43 samples as previously described (7). SthK currents were recorded from inside-out spheroplast patches using an Axopatch 200A amplifier with Patchmaster software (HEKA Elektronik) as previously described (7). The pipette and bath recording solution were both: 150 mM KCl, 20 mM $MgCl_2$, 500 mM sucrose, 10 mM HEPES, pH7.4 (7). Currents were measured using jumps in the holding potential from 0 mV to +80 mV. Fractional activation for 1 mM cGMP were obtained by comparing the fractional response to 1 mM cAMP in the same patch.

Statistics and reproducibility. Data values were expressed as mean ± SEM of n independent experiments, unless stated otherwise, and all error bars are ± SEM. Statistical significance (*P<0.05) was determined by using a two tailed Student's t-test.

Data Sharing Plan

Source data files will be included with the final submission. Code used for data analysis has been posted to https://github.com/zagotta/FDlifetime_program.

References:

1. K. B. Craven, W. N. Zagotta, CNG and HCN channels: Two peas, one pod. *Annu Rev Physiol* **68**, 375–401 (2006).

2. K. Matulef, W. N. Zagotta, Cyclic Nucleotide-Gated Ion Channels. *Annu Rev Cell Dev Biol* **19**, 23–44 (2003).

3. C. He, F. Chen, B. Li, Z. Hu, Neurophysiology of HCN channels: From cellular functions to multiple regulations. *Prog Neurobiol* **112**, 1–23 (2014).

4. U. B. Kaupp, R. Seifert, Cyclic Nucleotide-Gated Ion Channels. *Physiol Rev* **82**, 769–824 (2002).

5. Z. M. James, W. N. Zagotta, Structural insights into the mechanisms of CNBD channel function. *Journal of General Physiology* **150**, 225–244 (2018).

6. M. Brams, J. Kusch, R. Spurny, K. Benndorf, C. Ulens, Family of prokaryote cyclic nucleotide-modulated ion channels. *Proc Natl Acad Sci U S A* **111**, 7855–7860 (2014).

7. J. L. W. Morgan, E. G. B. Evans, W. N. Zagotta, Functional characterization and optimization of a bacterial cyclic nucleotide-gated channel. *Journal of Biological Chemistry* **294**, 7503–7515 (2019).

8. P. A. M. Schmidpeter, X. Gao, V. Uphadyay, J. Rheinberger, C. M. Nimigean, Ligand binding and activation properties of the purified bacterial cyclic nucleotide-gated channel SthK. *Journal of General Physiology* **150**, 821–834 (2018).

9. D. Kesters, *et al.*, Structure of the SthK carboxy-terminal region reveals a gating mechanism for cyclic nucleotide-modulated ion channels. *PLoS One* **10**, 1–12 (2015).

10. J. Rheinberger, X. Gao, P. A. M. Schmidpeter, C. M. Nimigean, Ligand discrimination and gating in cyclic nucleotide-gated ion channels from apo and partial agonist-bound cryo-EM structures. *Elife* **7**, 1–25 (2018).

11. X. Gao, *et al.*, Gating intermediates reveal inhibitory role of the voltage sensor in a cyclic nucleotide-modulated ion channel. *Nat Commun* **13** (2022).

12. H. A. DeBerg, P. S. Brzovic, G. E. Flynn, W. N. Zagotta, S. Stoll, Structure and energetics of allosteric regulation of HCN2 ion channels by cyclic nucleotides. *Journal of Biological Chemistry* **291**, 371–381 (2016).

13. A. Collauto, *et al.*, Rates and equilibrium constants of the ligand-induced conformational transition of an HCN ion channel protein domain determined by DEER spectroscopy. *Physical Chemistry Chemical Physics* **19**, 15324–15334 (2017).

14. D. Colquhoun, Binding, gating, affinity and efficacy: The interpretation of structure-activity relationships for agonists and of the effects of mutating receptors. *Br J Pharmacol* **125**, 923–947 (1998).

15. A. Auerbach, Life at the top: the transition state of AChR gating. *Sci STKE* **2003**, 1–9 (2003).

16. H. Y. Aviram, *et al.*, Direct observation of ultrafast large-scale dynamics of an enzyme under turnover conditions. *Proc Natl Acad Sci U S A* **115**, 3243–3248 (2018).

17. J. Guo, H. X. Zhou, Protein Allostery and Conformational Dynamics. *Chem Rev* **116**, 6503–6515 (2016).

18. F. T. Horrigan, R. W. Aldrich, Coupling between voltage sensor activation, Ca2+ binding and channel opening in large conductance (BK) potassium channels. *J Gen Physiol* **120**, 267–305 (2002).

19. H. Hofmann, All over or overall - Do we understand allostery? *Curr Opin Struct Biol* **83**, 102724 (2023).

20. W. N. Zagotta, *et al.*, An improved fluorescent noncanonical amino acid for measuring conformational distributions using time-resolved transition metal ion FRET. *Elife* **10**, 2021.05.10.443484 (2021).

21. S. E. Gordon, *et al.*, Long-distance tmFRET using bipyridyl- and phenanthroline-based ligands. *Biophys J* 2023.10.09.561591 (2024). https://doi.org/10.1016/j.bpj.2024.01.034.

22. W. N. Zagotta, *et al.*, Measuring conformational equilibria in allosteric proteins with time-resolved tmFRET. *Biophys J* 2023.10.09.561594 (2024). https://doi.org/10.1016/j.bpj.2024.01.033.

23. J. R. Lakowicz, *Principles of fluorescence spectroscopy* (2006).

24. I. Sungwienwong, *et al.*, Improving target amino acid selectivity in a permissive aminoacyl tRNA synthetase through counter-selection. *Org Biomol Chem* **15**, 3603–3610 (2017).

25. L. Stryer, R. P. Haugland, Energy transfer: a spectroscopic ruler. *Proc Natl Acad Sci U S A* **58**, 719–726 (1967).

26. M. H. Tessmer, S. Stoll, chiLife: An open-source Python package for in silico spin labeling and integrative protein modeling. *PLoS Comput Biol* **19**, 1–16 (2023).

27. L. C. Speight, *et al.*, Efficient synthesis and in vivo incorporation of acridon-2-ylalanine, a fluorescent amino acid for lifetime and Förster resonance energy transfer/luminescence resonance energy transfer studies. *J Am Chem Soc* **135**, 18806–18814 (2013).

28. M. A. Digman, V. R. Caiolfa, M. Zamai, E. Gratton, The phasor approach to fluorescence lifetime imaging analysis. *Biophys J* **94**, 14–16 (2008).

29. M. Lolicato, *et al.*, Tetramerization dynamics of C-terminal domain underlies isoform-specific cAMP gating in hyperpolarization-activated cyclic nucleotide-gated channels. *Journal of Biological Chemistry* **286**, 44811–44820 (2011).

30. K. B. Craven, W. N. Zagotta, Salt bridges and gating in the COOH-terminal region of HCN2 and CNGA1 channels. *J Gen Physiol* **124**, 663–677 (2004).

31. J. W. Taraska, M. C. Puljung, N. B. Olivier, G. E. Flynn, W. N. Zagotta, Mapping the structure and conformational movements of proteins with transition metal ion FRET. *Nat Methods* **6**, 532–537 (2009).

32. K. Matulef, W. N. Zagotta, Multimerization of the ligand binding domains of cyclic nucleotide-gated channels. *Neuron* **36**, 93–103 (2002).

33. M. C. Puljung, H. A. DeBerg, W. N. Zagotta, S. Stoll, Double electron - Electron resonance reveals cAMP-induced conformational change in HCN channels. *Proc Natl Acad Sci U S A* **111**, 9816–9821 (2014).

34. E. G. B. Evans, J. L. W. Morgan, F. DiMaio, W. N. Zagotta, S. Stoll, Allosteric conformational change of a cyclic nucleotide-gated ion channel revealed by DEER spectroscopy. *Proc Natl Acad Sci U S A* **117**, 10839–10847 (2020).

35. M. P. Goldschen-Ohm, *et al.*, Structure and dynamics underlying elementary ligand binding events in human pacemaking channels. *Elife* **5** (2016).

36. C. Pfleger, *et al.*, Allosteric signaling in C-linker and cyclic nucleotide-binding domain of HCN2 channels. *Biophys J* **120**, 950–963 (2021).

37. K. B. Craven, N. B. Olivier, W. N. Zagotta, C-terminal movement during gating in cyclic nucleotide-modulated channels. *J Biol Chem* **283**, 14728–14738 (2008).

38. M. Kondapuram, *et al.*, Functional and structural characterization of interactions between opposite subunits in HCN pacemaker channels. *Commun Biol* **5**, 1–14 (2022).

39. S. E. Gordon, W. N. Zagotta, A histidine residue associated with the gate of the cyclic nucleotide-activated channels in rod photoreceptors. *Neuron* **14**, 177–183 (1995).

40. M. D. Varnum, K. D. Black, W. N. Zagotta, Molecular mechanism for ligand discrimination of cyclic nucleotide-gated channels. *Neuron* **15**, 619–625 (1995).

41. M. P. Goldschen-Ohm, D. S. White, V. A. Klenchin, B. Chanda, R. H. Goldsmith, Observing Single-Molecule Dynamics at Millimolar Concentrations. *Angew Chem Int Ed Engl* **56**, 2399–2402 (2017).

42. H. Liu, J. H. Naismith, An efficient one-step site-directed deletion, insertion, single and multiple-site plasmid mutagenesis protocol. *BMC Biotechnol* **8**, 91 (2008).

43. I. Sungwienwong, *et al.*, Improving target amino acid selectivity in a permissive aminoacyl tRNA synthetase through counter-selection. *Org Biomol Chem* **15**, 3603–3610 (2017).

44. T. Mukai, *et al.*, Highly reproductive Escherichia coli cells with no specific assignment to the UAG codon. *Sci Rep* **5**, 1–9 (2015).

45. C. M. Jones, Y. Venkatesh, E. J. Petersson, *Protein labeling for FRET with methoxycoumarin and acridonylalanine*, 1st Ed. (Elsevier Inc., 2020).

46. D. Wu, G. Piszczek, Standard protocol for mass photometry experiments. *Eur Biophys J* **50**, 403–409 (2021).

47. G. Young, *et al.*, Quantitative mass imaging of single biological macromolecules. *Science* **360**, 423–427 (2018).

48. J. R. Lakowicz, *et al.*, Resolution of the conformational distribution and dynamics of a flexible molecule using frequency-domain fluorometry. *Biophys Chem* **39**, 79–84 (1991).

49. H. C. Cheung, *et al.*, Conformational flexibility of the Cys 697-Cys 707 segment of myosin subfragment-1: Distance distributions by frequency-domain fluorometry. *Biophys Chem* **40**, 1–17 (1991).

50. J. R. Lakowicz, *et al.*, Distance distributions in proteins recovered by using frequency-domain fluorometry. Applications to troponin I and its complex with troponin C. *Biochemistry* **27**, 9149–9160 (1988).

51. R. A. Hochstrasser, S. M. Chen, D. P. Millar, Distance distribution in a dye-linked oligonucleotide determined by time-resolved fluorescence energy transfer. *Biophys Chem* **45**, 133–141 (1992).

52. T. Kawate, E. Gouaux, Fluorescence-detection size-exclusion chromatography for precrystallization screening of integral membrane proteins. *Structure* **14**, 673–681 (2006).

53. B. Miroux, J. E. Walker, Over-production of proteins in Escherichia coli: mutant hosts that allow synthesis of some membrane proteins and globular proteins at high levels. *J Mol Biol* **260**, 289–298 (1996).
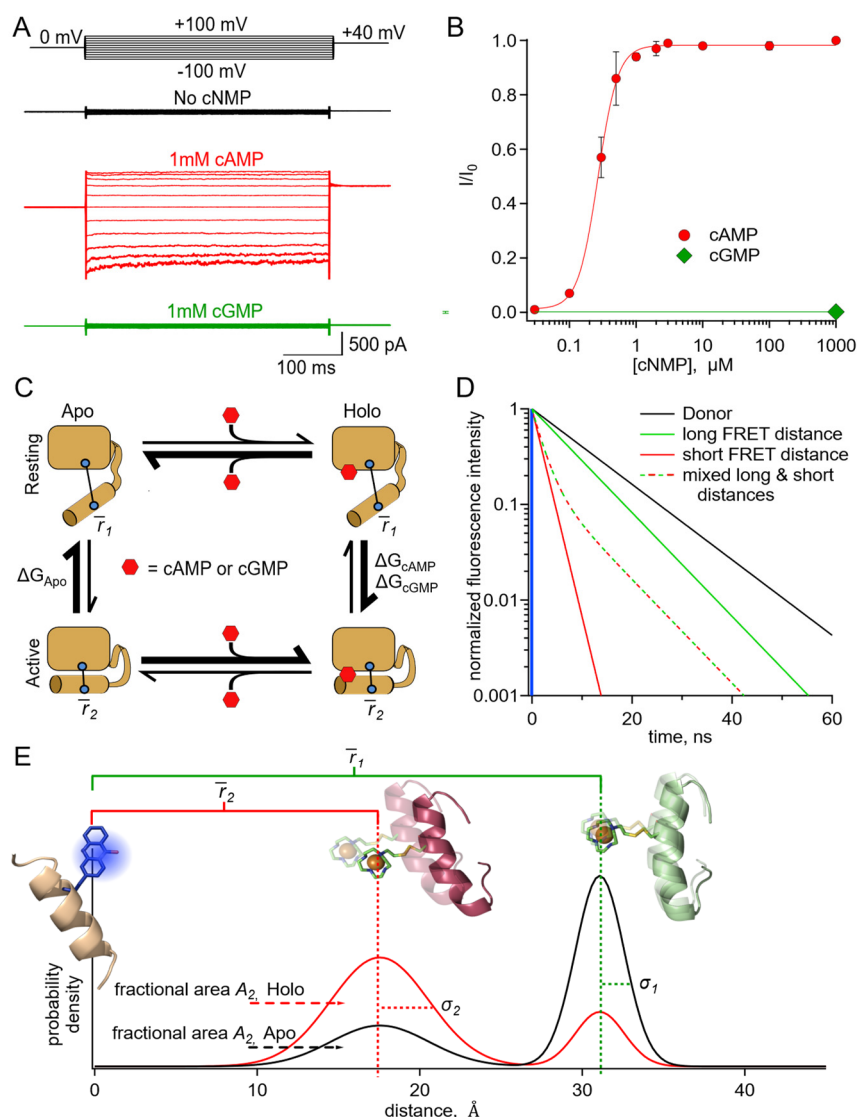
Figures

Fig. 1. SthK as a model protein for characterizing the allosteric regulation in CNBD channels. **(A)** Representative macroscopic A208V-cfSthK currents in inside-out patches from bacterial spheroplasts in response to voltage steps shown at the top, in the absence of cyclic nucleotide (top black trace), in saturating 1 mM cAMP (middle red trace), and in saturating 1 mM cGMP (bottom green trace). **(B)** Dose-response relation of A208V-cfSthK to cAMP at +80 mV (red circles, n=6), fit with the Hill Equation (in red, $K_{1/2}$: 0.27 ± 0.01 µM, slope: 2.9 ± 0.2, $\pm$ SD). Fractional activation by 1 mM cGMP was 0.002 ± 0.003 ($\pm$ SD) (green diamond, n=6). **(C)** State diagram showing four states (either apo or holo, and either resting or active) of the CNBD and the associated ΔG's for the transitions between states. **(D)** Theoretical fluorescence lifetime decays of a donor fluorophore in the time-domain showing basis of time-resolved tmFRET. A single exponential donor and mixtures of two single tmFRET distances (short and long) are shown. **(E)** Theoretical distance distributions showing two states with average distances, $\bar{r}$, heterogeneity within each conformational state as standard deviation, σ, and heterogeneity between conformational states as fractional area A_2 for apo (black) and holo (red) conditions.
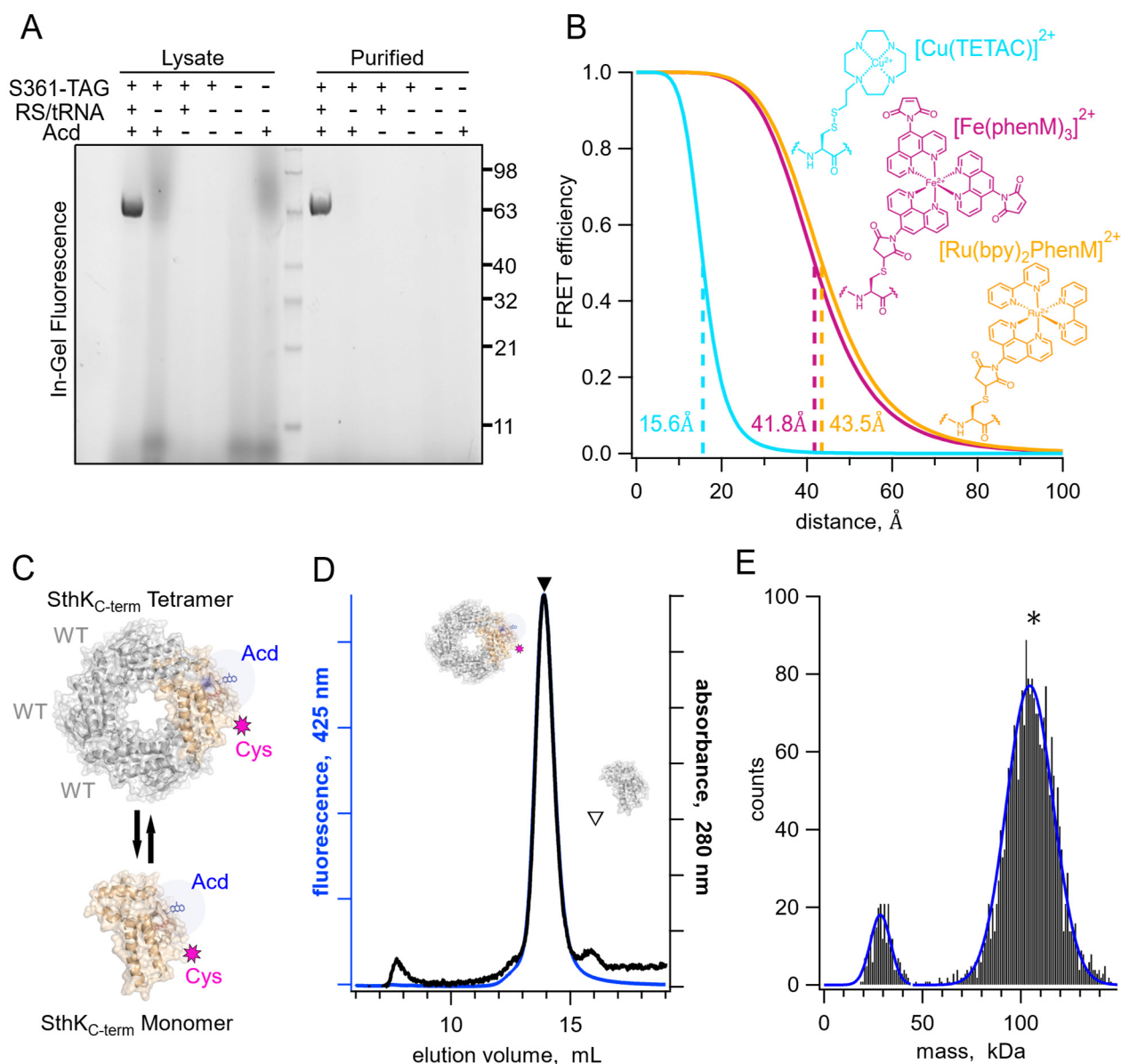
21

Fig. 2. Expression, purification, and tetrameric analysis of SthK_{C-term}. **(A)** In-gel protein fluorescence showing selective Acd incorporation into SthK_{C-term} in the absence and presence of S361Acd TAG site, Acd aminoacyl tRNA synthetase/tRNA (RS/tRNA), and unnatural amino acid Acd. **(B)** Structures of cysteine modified by acceptor compounds $[Cu(TETAC)]^{2+}$ (cyan), $[Fe(phenM)_3]^{2+}$ (magenta), and $[Ru(bpy)_2phenM]^{2+}$ (orange) along with their corresponding Förster curves of FRET efficiency as a function of distance from Acd, and their R_0 values specified and marked with dashed lines. **(C)** SthK_{C-term} cartoon as tetramer and monomer showing WT subunits in gray and cysteine-containing Acd-labeled subunits in orange. **(D)** SEC traces (absorbance at 280 nm in black and 425 nm fluorescence emission for Acd in blue) of isolated WT-Acd-heterotetrameric protein (closed triangle) vs monomeric WT protein (open triangle). **(E)** Mass photometry histogram data showing primarily tetramers, with single Gaussian fits (blue, 29 kDa ± 7.3 and 104.5 kDa ± 16.8, ± SD).
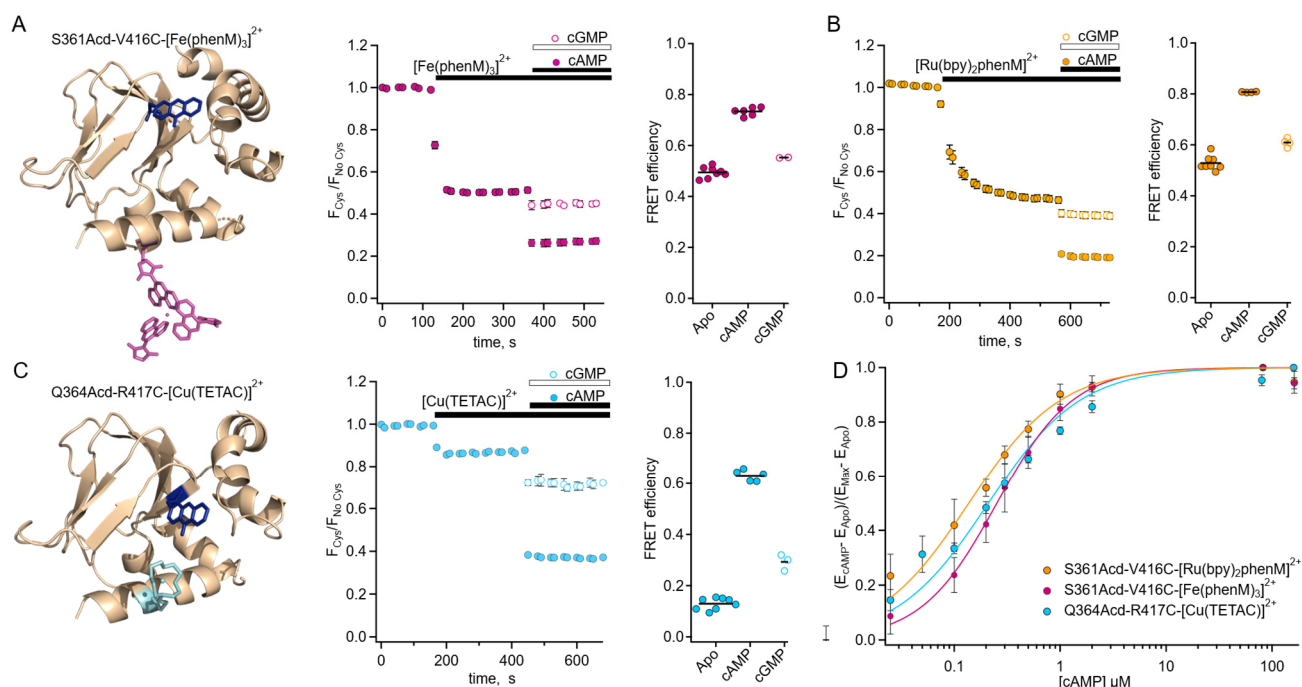
22

Fig. 3. Steady-state tmFRET data from tetrameric SthK$_{C\text{-term}}$. **(A)** Left: structure of one subunit of SthK$_{C\text{-term}}$-S361Acd with [Fe(phenM)$_3$]$^{2+}$ acceptor incorporated at V416C (adapted from PDB: 4D7T) (9). Middle: averaged fluorescence time course upon addition of [Fe(phenM)$_3$]$^{2+}$ and then cAMP or cGMP (apo, n=8; cAMP n=6; and cGMP, n=2). Right: summary of the FRET efficiencies from individual experiments, with mean values as horizontal lines. **(B)** Left: Average fluorescence time course for same site upon addition of [Ru(bpy)$_2$phenM]$^{2+}$ acceptor and then cAMP or cGMP (apo, n=8; cAMP, n=4; and cGMP, n=4). Right: summary of FRET efficiencies, with mean values as horizontal lines. **(C)** Left: structure of one subunit of SthK$_{C\text{-term}}$-Q364Acd-417C with [Cu(TETAC)]$^{2+}$ acceptor incorporated at R417C. Middle: averaged fluorescence time course upon addition of [Cu(TETAC)]$^{2+}$ then cAMP or cGMP (apo, n= 8; cAMP, n=5; and cAMP, n=3). Right: summary of FRET efficiencies, with mean values as horizontal lines. **(D)** Dose response relations of FRET efficiency change as a function of cAMP concentration normalized for comparison and fit with Hill equations ($K_{1/2}$: 0.25 ± 0.01 μM , 0.14 ± 0.01 μM, 0.21 ± 0.02 μM, and h:1.2 ± 0.07, 1, and 1 for [Fe(phenM)$_3$]$^{2+}$, magenta; [Ru(bpy)$_2$phenM]$^{2+}$, orange; and [Cu(TETAC)]$^{2+}$, cyan respectively, ± SD).
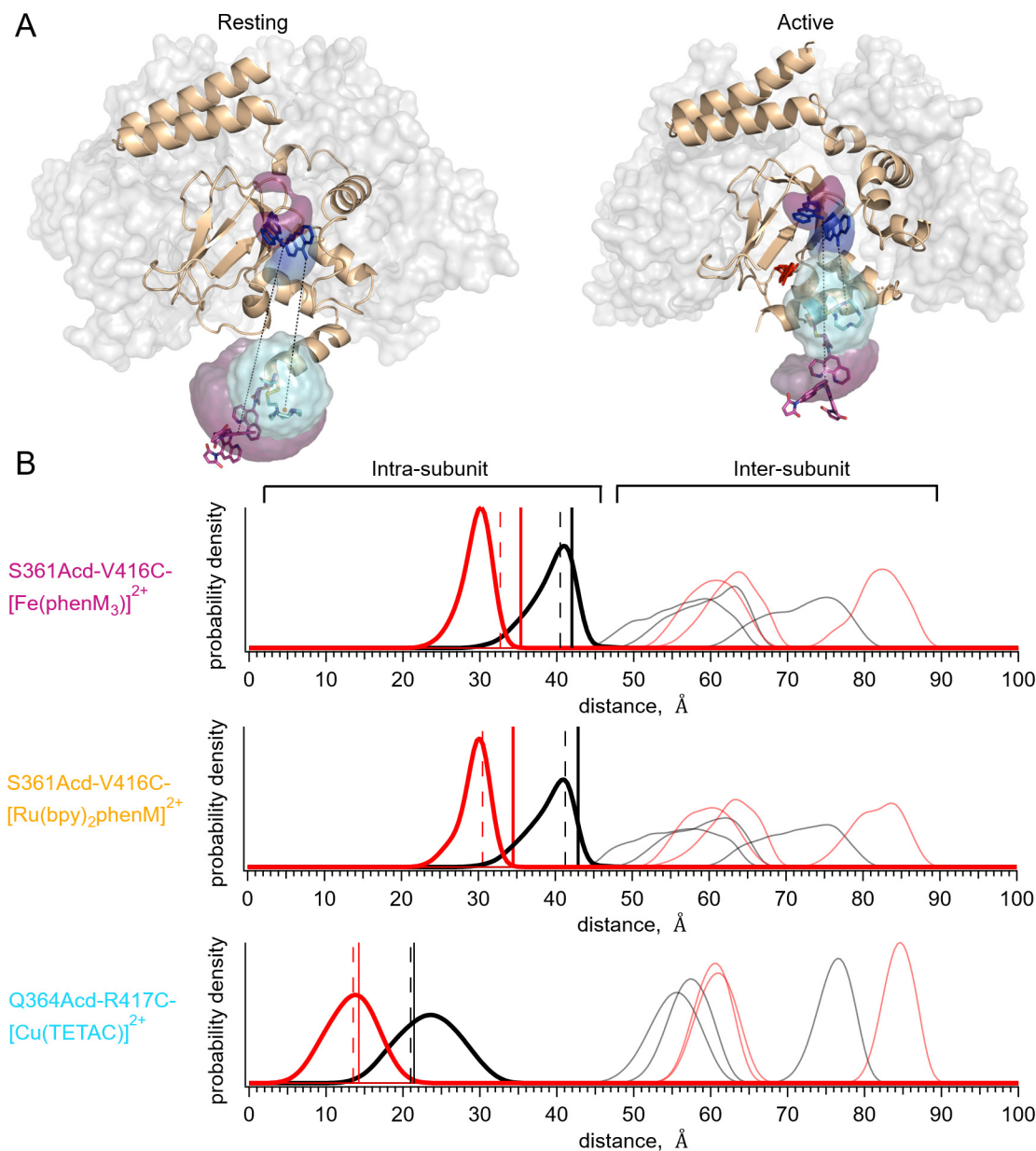
23

Fig. 4. Distance distribution predictions with chiLife. **(A)** Structure of resting state (left, PDB:7RSH) (11), and cAMP-bound active state (right, PDB:4D7T) (9) with rotameric clouds predicted by chiLife for the labels (Acd, blue; $[Fe(phenM)_3]^{2+}$, magenta; and $[Cu(TETAC)]^{2+}$, cyan). Gray surface indicates location of adjacent WT subunits in tetramer. **(B)** Distance distributions predicted by chiLife for $SthK_{C\text{-term}}$-S361Acd-V416C-$[Fe(phenM)_3]^{2+}$, $SthK_{C\text{-term}}$-S361Acd-V416C-$[Ru(bpy)_2phenM]^{2+}$ and $SthK_{C\text{-term}}$-Q364Acd-R417C-$[Cu(TETAC)]^{2+}$ (intra-subunit distances: resting, black curves; active, red curves; and inter-subunit distances: resting, grey curves; active, pink curves). Average steady-state tmFRET distance measurements are overlaid as vertical lines for data from Figure 3 (apo, solid black, and cAMP, solid red) and adjusted assuming a 10% unlabeled protein (dashed black and red vertical lines).
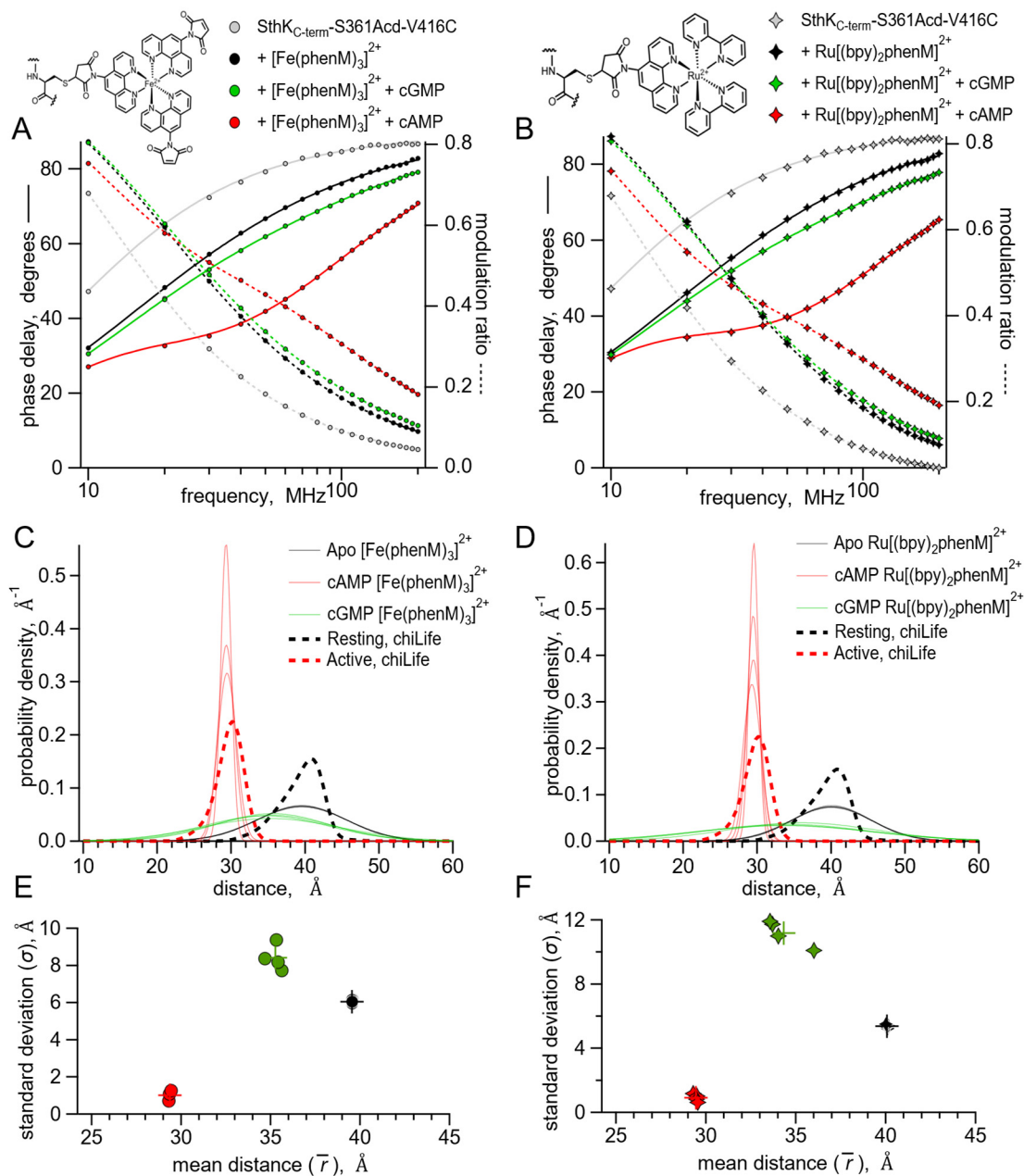
24

Fig. 5. Lifetime measurements of SthK$_{C\text{-term}}$-S361Acd-V416C with [Fe(phenM)$_3$]$^{2+}$ and [Ru(bpy)$_2$phenM]$^{2+}$. Chemical structures of acceptors and legends for all plots shown on top. **(A-B)** Representative Weber plots of phase delay and modulation ratio for SthK$_{C\text{-term}}$-S361Acd-V416C labeled with [Fe(phenM)$_3$]$^{2+}$ (A) and [Ru(bpy)$_2$phenM]$^{2+}$(B). Fits of the data using the single Gaussian model are shown with phase delay as solid curves and modulation ratio as dashed curves. **(C-D)** Spaghetti plots showing distance distributions from the model fits with apo (thin black curves, n=4), with 1.23 mM cAMP (thin red curves, n=4) and 1.23 mM cGMP (thin green curves, n=4) for [Fe(phenM)$_3$]$^{2+}$ (C) and [Ru(bpy)$_2$phenM]$^{2+}$(D). Distributions predicted by chiLife are overlayed in dashed curves. **(E-F)** Summary of Gaussian fit standard deviations, σ, versus average distances, $\bar{r}$, for [Fe(phenM)$_3$]$^{2+}$ (E) and [Ru(bpy)$_2$phenM]$^{2+}$ (F), with average values as cross marks.
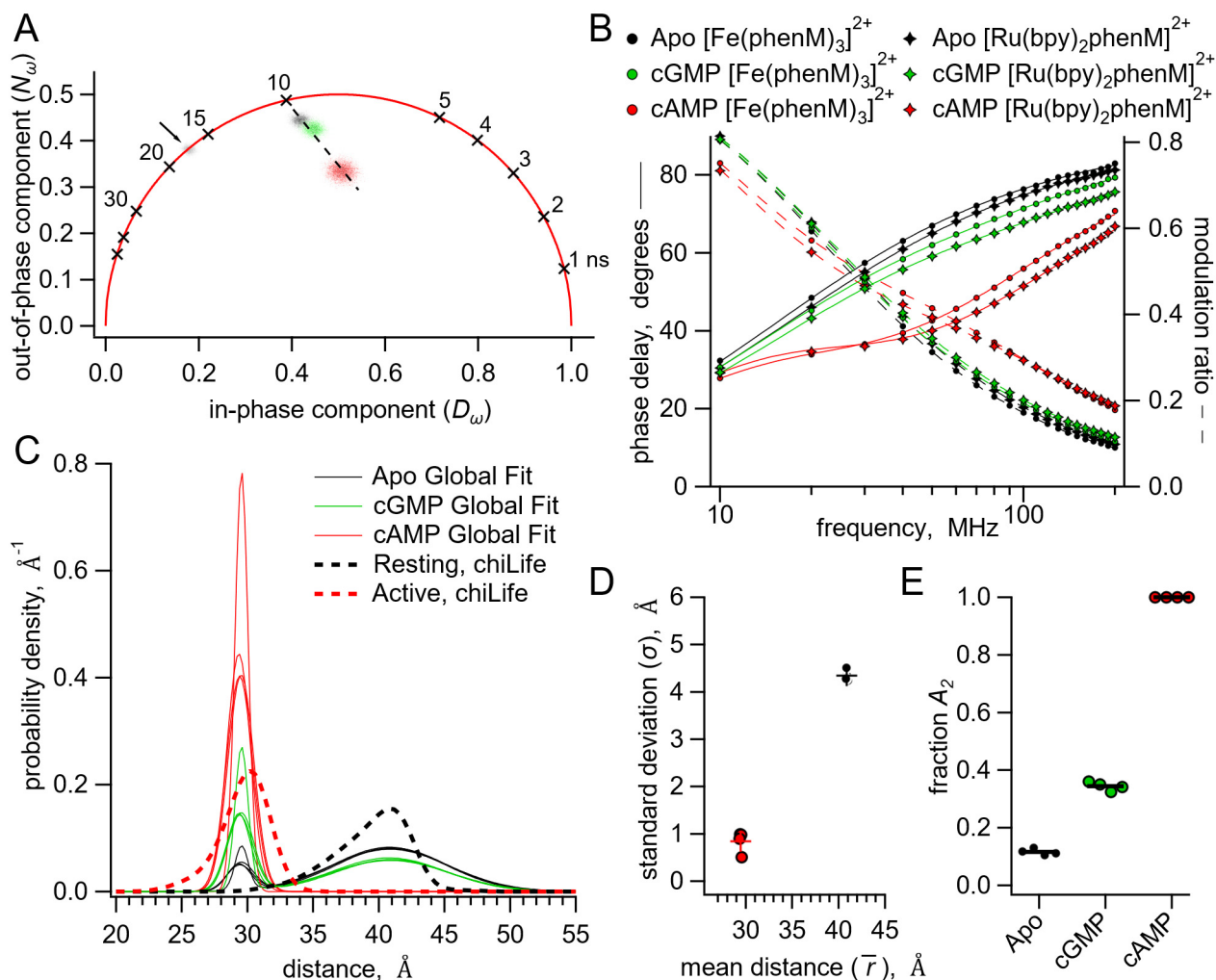
25

Fig. 6. Analysis of lifetime data with global fit model allowing sum of two Gaussian distance distributions. **(A)** Representative phasor plot of measured lifetimes with $[Fe(phenM)_3]^{2+}$ acceptor, where markers on universal circle indicate single-exponential time constants (in nanoseconds). Data shown are donor-only *(*grey), apo (black), cAMP (red*)* and cGMP (green). **(B)** Representative Weber plot showing global fits for $[Fe(phenM)_3]^{2+}$ acceptor data (closed circles) and $[Ru(Bpy)_2phenM]^{2+}$ acceptor data (open diamonds) for apo (black), cAMP (red) and cGMP (green) conditions. **(C)** Spaghetti plot of distance distributions for each experiment (n=4) (thin lines). For comparison, chiLife distributions are overlayed (dashed curves). **(D)** Summary of Gaussian fit standard deviations, σ, versus average distances, $\bar{r}$, for apo and cAMP, with average values as cross marks. Colors correspond to conditions in (A-C). **(E)** Fit values and averages for fraction activation (A_2) for each condition.
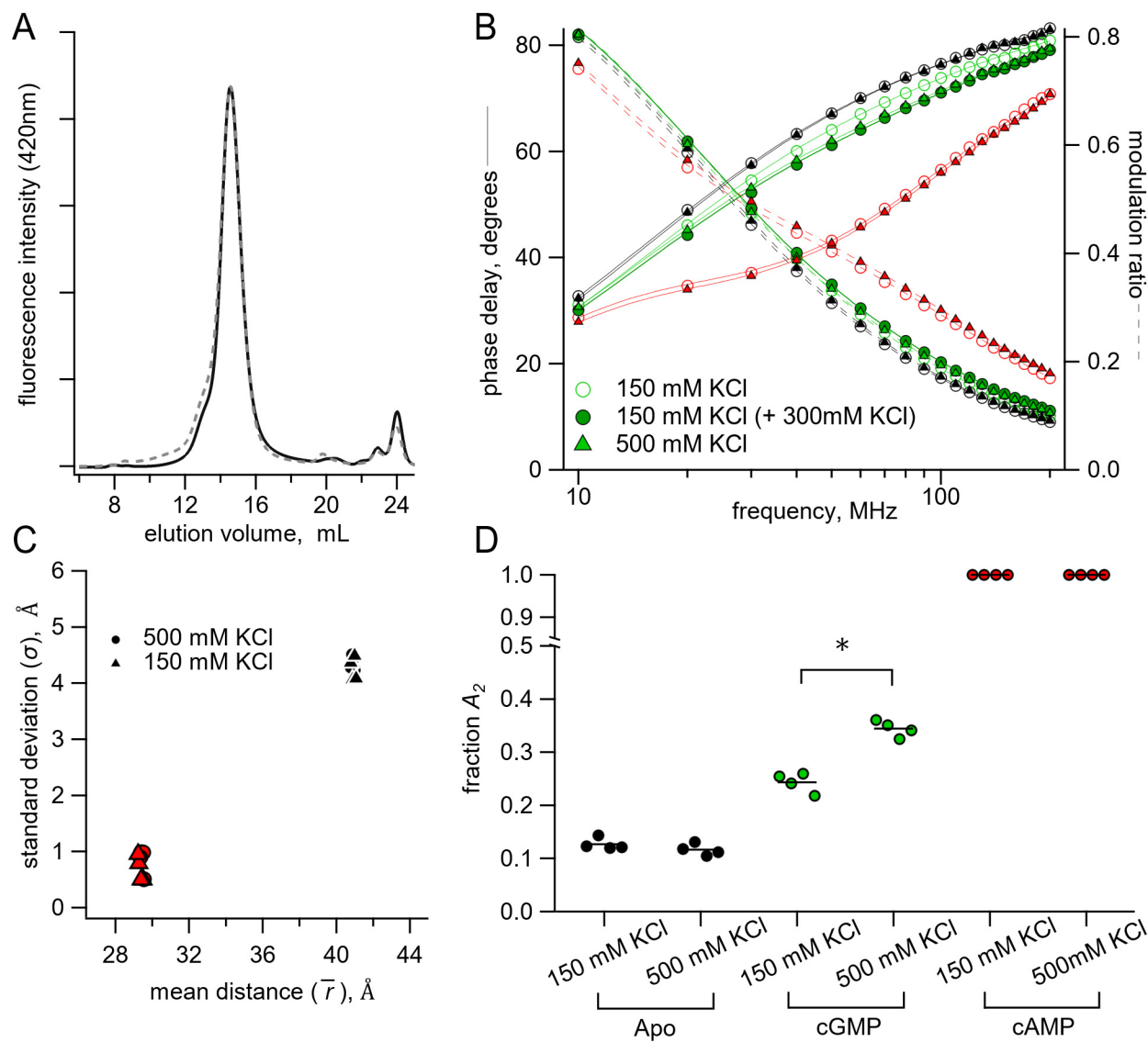
Fig. 7. Lifetime measurements in 150 mM KCl versus 500 mM KCl conditions. **(A)** Normalized SEC traces of SthK$_{C-term}$ in 150 mM KCl (solid curve) and 500 mM KCl (dashed curve). **(B)** Representative Weber plot for [Fe(phenM)$_3$]$^{2+}$ lifetimes in 150 mM (open circles) and 500 mM KCl (closed triangles), in each ligand condition (apo, black; cGMP, green; cAMP; red). An additional lifetime trace is shown for an experiment where additional 300 mM KCl was added to the protein sample with 150 mM KCl in cGMP (closed green circles). **(C)** Comparison of Gaussian average distance, $\bar{r}$, and standard deviation, σ, between ionic concentrations using model global fitting of [Fe(phenM)$_3$]$^{2+}$ and [Ru(bpy)$_2$phenM]$^{2+}$ with the sum of two Gaussians (apo, black, and cAMP, red, n=4). **(D)** Fraction of active state in each condition (A_2) for 150 mM KCl and 500 mM KCl using the sum of two Gaussian model fits [apo P=0.2, cGMP *P=0.0001].

27

Table 1. Calculated Energetics of the Four State Model

Ligand Condition	Ionic Strength (mM KCl)	ΔG (kcal/mol)	$\Delta\Delta G$ (kcal/mol)
Apo	150	1.14 ± 0.03	--
	500	1.2 ± 0.03	--
cAMP	150	--	--
	500	$< -2.7 \pm 0$	$< -3.9 \pm 0.03$
cGMP	150	0.67 ± 0.03	-0.47 ± 0.04
	500	0.38 ± 0.02	-0.82 ± 0.04

Energies are reported in mean values $\pm$ SEM.

Supplemental Figures
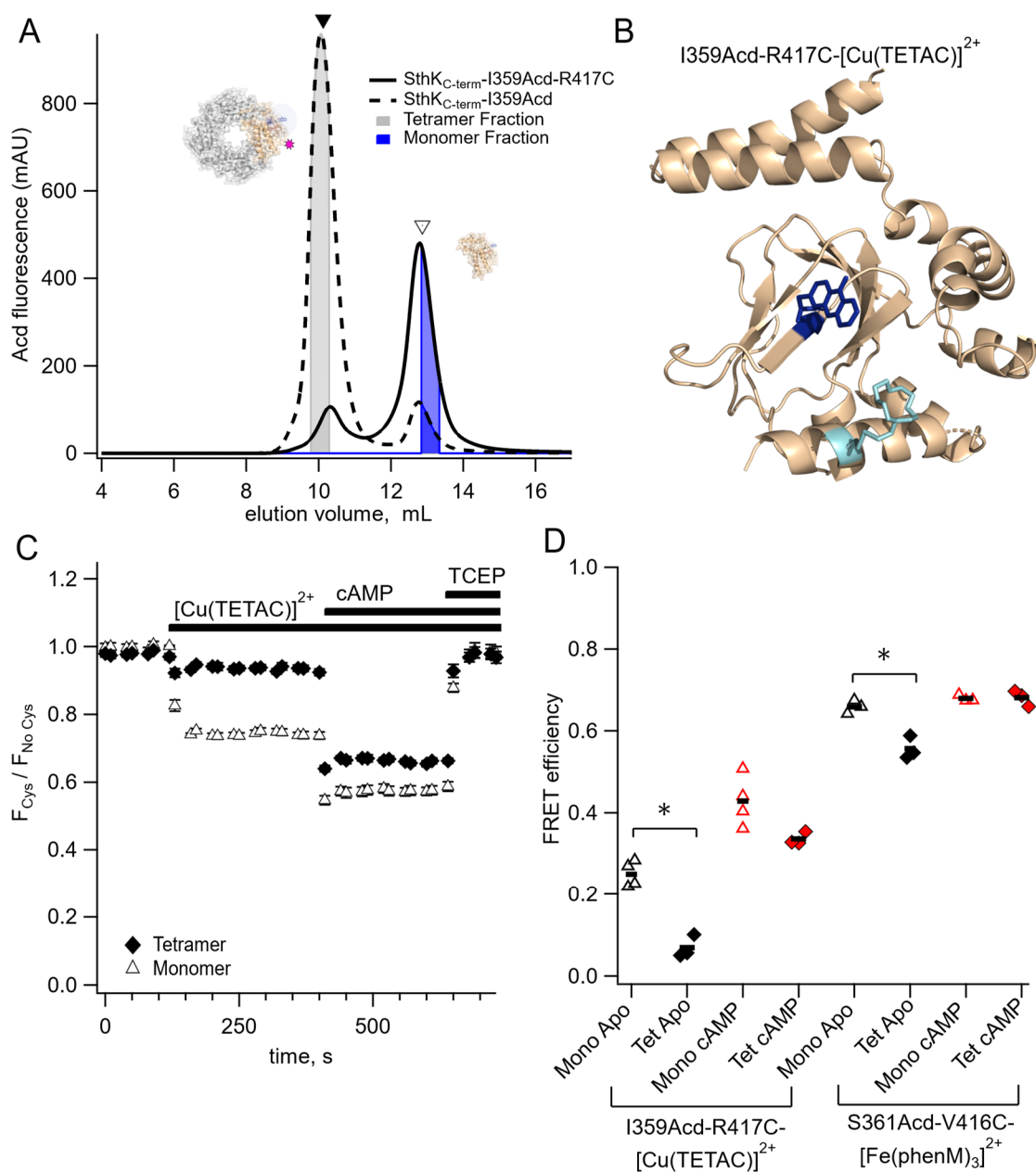
Fig. S1. Steady-state tmFRET of monomeric and tetrameric SthK$_{C-term}$. **(A)** SEC chromatogram showing separation of monomeric (empty triangle, blue area) and tetrameric protein (solid triangle, gray area) fractions for SthK$_{C-term}$-I359Acd and SthK$_{C-term}$-I359Acd-R417C (no WT SthK$_{C-term}$ present) on a Superdex 75 increase 10/300 column (GE Healthcare). **(B)** Structure showing SthK$_{C-term}$-I359Acd with [Cu(TETAC)]$^{2+}$ acceptor at R417C (PDB:4D7T). **(C)** Fluorescence time-course of SthK$_{C-term}$-I359Acd-417C upon addition of [Cu(TETAC)]$^{2+}$, cAMP and TCEP in tetrameric protein (closed diamonds) and monomeric protein (open triangles). **(D)** Summary of FRET efficiencies for monomer and tetramer, with mean values shown as horizontal lines. Left: SthK$_{C-term}$-I359Acd-R417C-[Cu(TETAC)]$^{2+}$ (apo, *P=0.0005, cAMP, P=0.06). Right: SthK$_{C-term}$-S361Acd-V416C-[Fe(phenM)$_3$]$^{2+}$ apo, *P=0.006, cAMP: P=0.9).
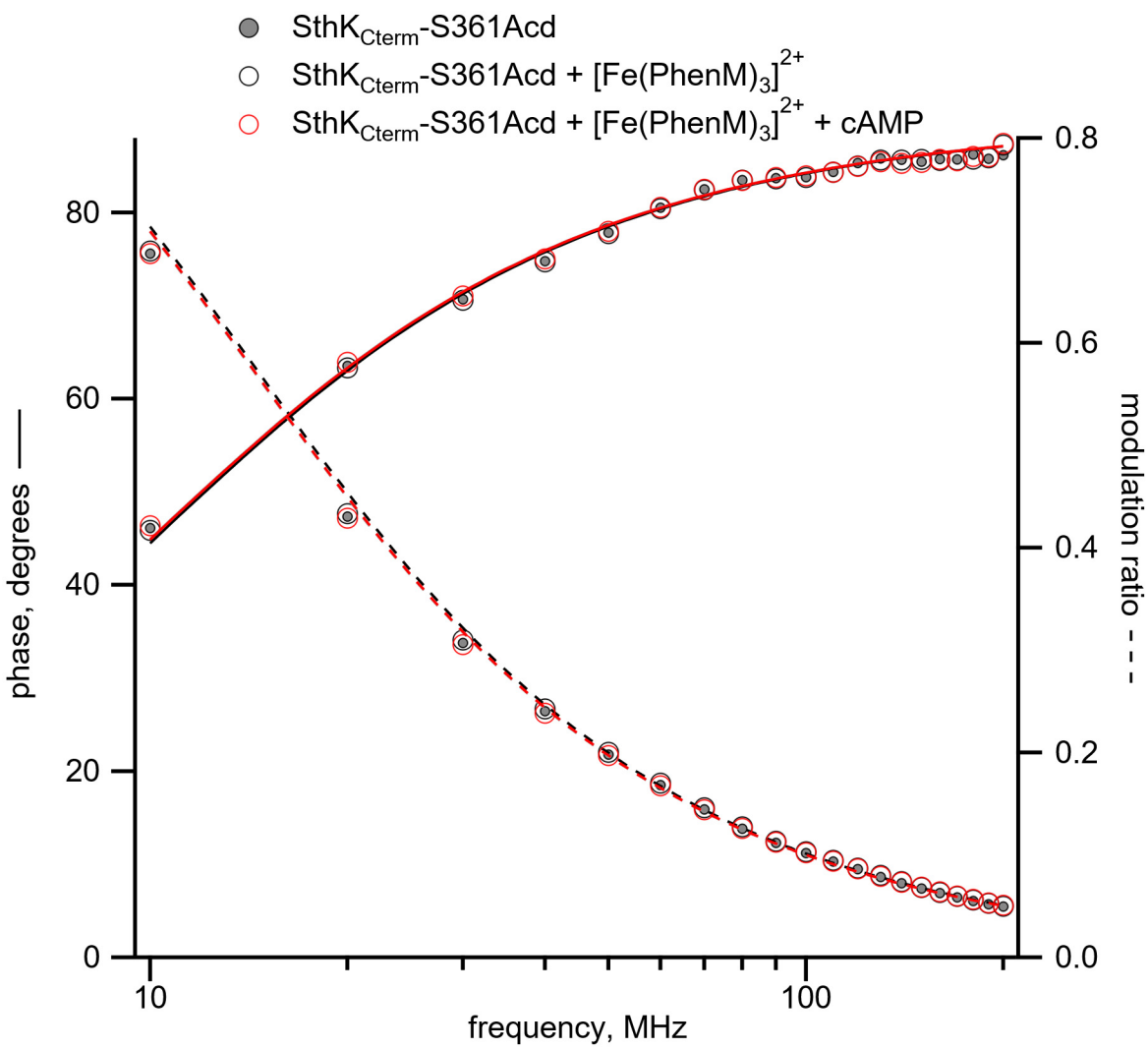
29

Fig. S2. Representative Weber plot of measured lifetimes of SthK$_{C-term}$-S361Acd donor-only (grey), then in the presence of [Fe(phenM)$_3$]$^{2+}$ (black), and after the addition of 1.23 mM cAMP (red), showing no change in lifetimes in the absence of a cysteine residue.
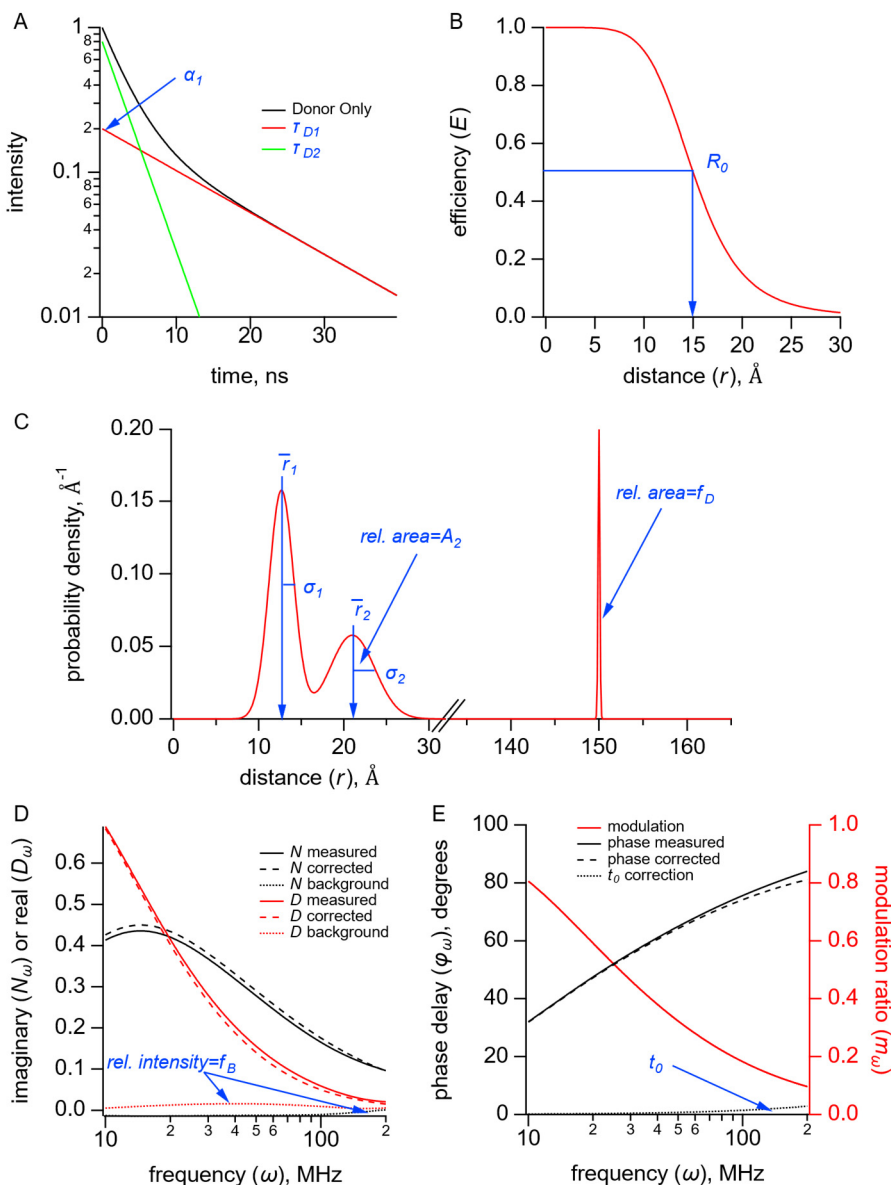
Fig. S3. Parameters used in the lifetimes fitting model for both the single and sum of two Gaussian approaches, shown in blue. **(A)** Graph of donor-only fluorescence-lifetime decay with two exponential components with time constants (τ_{D1}, τ_{D2}) **(B)** FRET efficiency (E) plot as a function of distance (r) between donor and acceptor and the R_0 values for 50% FRET transfer. **(C)** Probability distribution plot of donor and acceptor distances P(r) showing the sum of two Gaussian distributions, each with their own average distance ($\bar{r}_1$ and $\bar{r}_2$), standard deviations (σ_1 and σ_2) and relative amplitude of the second component (A_2). The donor-only fraction (f_D) is modeled as a narrow Gaussian with mean distance of 150 Å and standard deviation of 0.1 Å, beyond a detectable amount of FRET. **(D)** The in-phase (D_ω) and out-of-phase (N_ω) components are plotted for the measured, corrected, and background fluorescence signal as a function of the excitation modulation frequency (ω), where f_B is the fraction of the fluorescence intensity due to the background. **(E)** Plot of the phase delay (φ_ω) and modulation ratio (m_ω) of the measured and corrected fluorescence response as a function of the modulation frequency (ω) where t_0 is the time shift of the instrument response function.
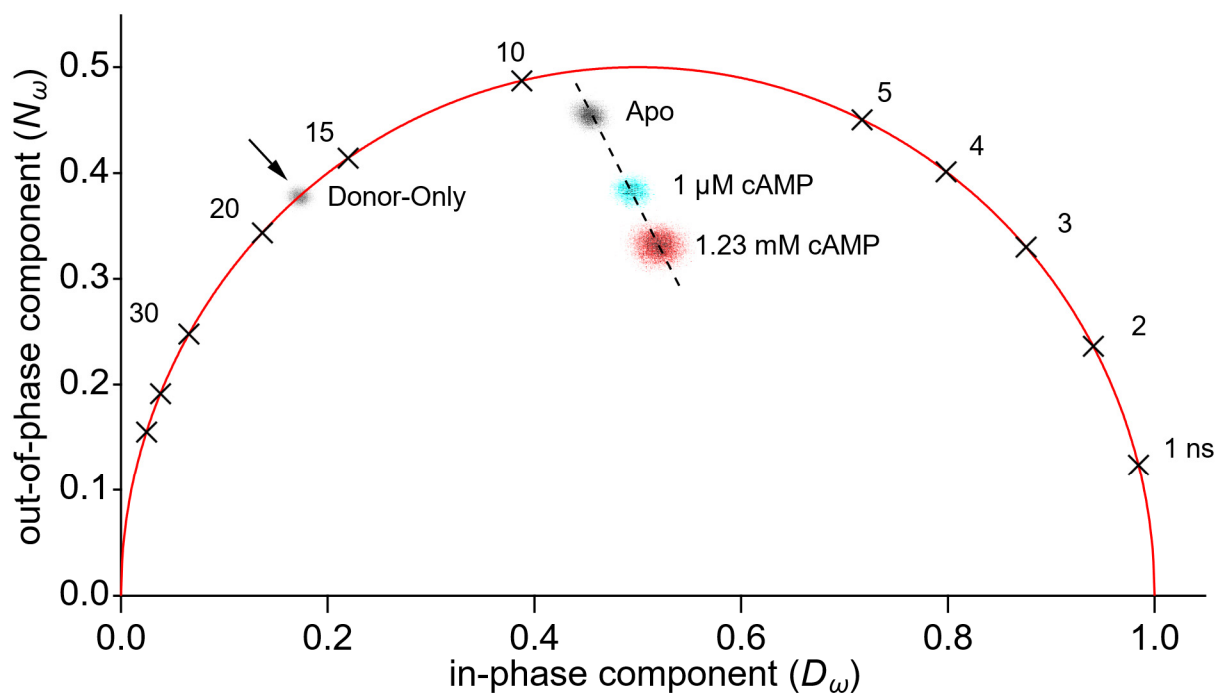
Fig. S4. Representative phasor plot of measured lifetimes of SthK$_{C-term}$-S361Acd-V416C alone (donor-only, grey), in the presence of [Ru(bpy)$_2$phenM]$^{2+}$ (apo, black), in the presence of 1 µM cAMP (cyan) and presence of 1.23 mM cAMP (red).

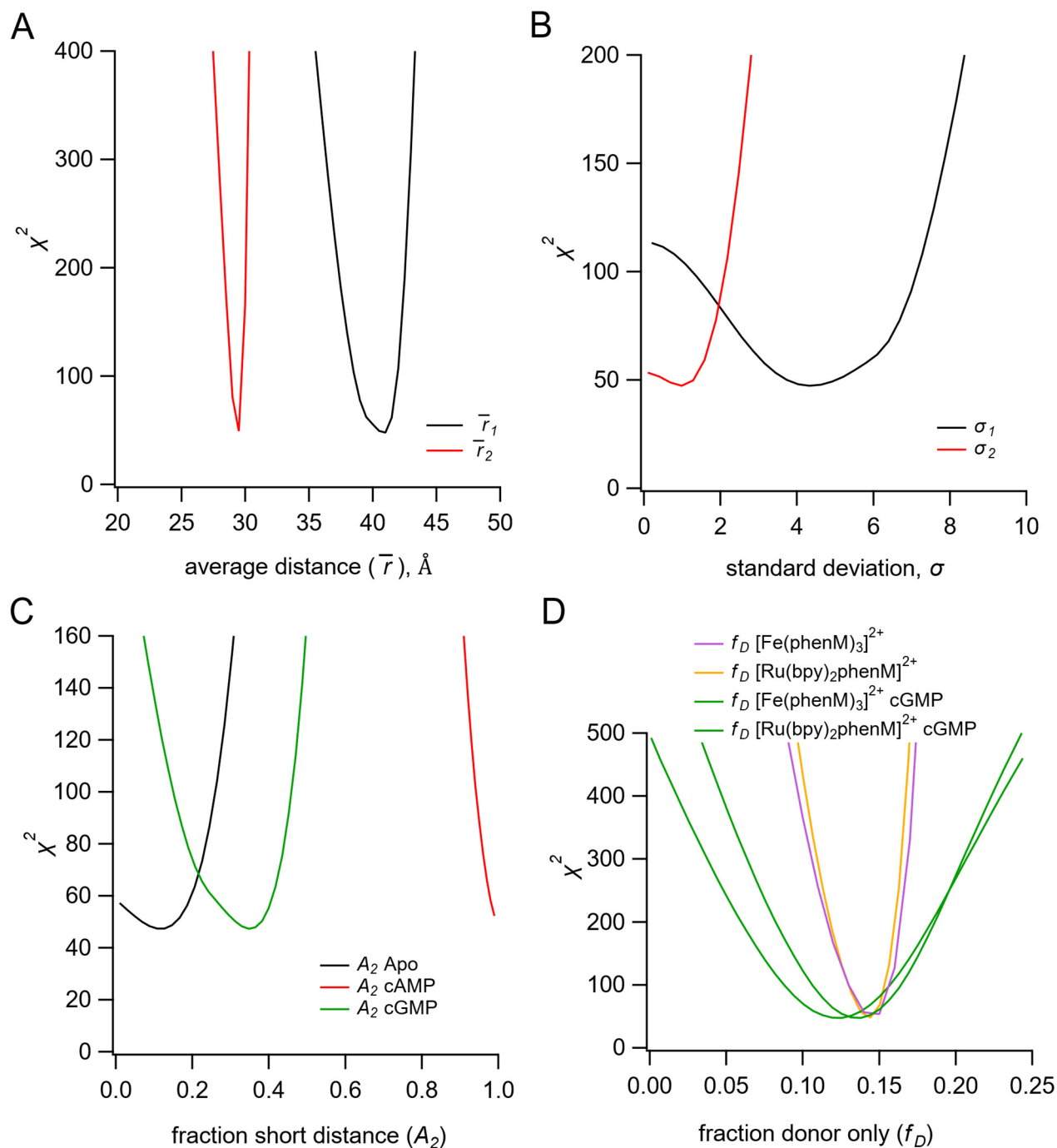**Fig. S5.** Identifiability of parameters in the sum of two Gaussian distributions model, with global fitting $Fe(phenM)_3]^{2+}$ and $[Ru(bpy)_2phenM]^{2+}$ data. **(A-B)** Minimization of χ^2 values for the Gaussian average distance ($\bar{r}$) (A) and standard deviation (σ) (B) for the resting (black) and active states (red). **(C)** Minimization of χ^2 values for parameter A_2 for the conditions of apo, cAMP and cGMP. **(D)** Minimization of χ^2 values for the fraction of donor-only component (f_D) in protein samples for each experiment of apo and cAMP for $[Fe(phenM)_3]^{2+}$, of apo and cAMP for $[Ru(bpy)_2phenM]^{2+}$, of cGMP for $[Fe(phenM)_3]^{2+}$, and of cGMP for $[Ru(bpy)_2phenM]^{2+}$.

33